DIPLOMARBEIT

Fabrication of High Finesse Mirrors for a Fiber Fabry-Pérot Cavity Experiment

zur Erlangung des akademischen Grades
Diplom-Ingenieur

im Rahmen des Studiums
Technische Physik

eingereicht von
Matthias Michalek, BSc
Matr. Nr.: 11702840

ausgeführt am Atominstitut
der Fakultät für Physik
der Technischen Universität Wien

unter der Betreuung von
Assistant Prof. Dr. Julian Léonard

Wien am 18.12.2024

Unterschrift StudentIn

Unterschrift BetreuerIn

Abstract

Fabry-Pérot resonators are vital tools for high-precision measurements due to their high spectral resolution and low loss rates. Recently, they have gained popularity in cavity quantum electrodynamics experiments. The high finesse and small mode volumes of fiber cavities provide strong coupling between cavity fields and atoms, enabling the study of atom-light entanglement and cavity-mediated interactions. In fiber-based cavities the mirrors are directly fabricated on the end faces of optical fibers. Fiber cavities offer multiple advantages like smaller mode volumes and easier integration with fiber-based control and readout systems. This work explores the most commonly used method for fabricating fiber mirrors using a CO_2-laser. The high power laser ablatively removes material from the fiber end face creating high quality mirror surfaces with a customizable geometry. A white light interferometer is used for in-situ profilometry and characterization of the produced structures. This work gives a detailed description of the production process and studies the effects of various production parameters on the geometry and quality of the final mirror surfaces. Our results set the stage for achieving high-quality fiber mirror machining surpassing the current state of the art.

Zusammenfassung

Fabry-Pérot-Resonatoren sind auf Grund ihrer hohen spektrale Auflösung und geringer optischer Verluste essenzielle Bausteine in einer Vielzahl von hochpräzisen optischen Instrumenten. In den letzten Jahren werden sie vermehrt in Experimenten der Resonator-Quantenelektrodynamik eingesetzt. Die hohe Finesse und kleinen Modenvolumen von Fabry-Pérot-Resonatoren ermöglichen starke Kopplungen zwischen dem Resonatorfeld und Atomen. So können Atom-Licht-Verschränkung und resonatorvermittelten Wechselwirkungen im Rahmen der Resonator-Quantenelektrodynamik experimentell untersucht werden. Bei faserbasierten Resonatoren werden die Resonatorspiegel direkt auf den Endflächen optischer Fasern gefertigt. Dies bietet mehrere Vorteile, wie kleine Modenvolumen und eine einfachere Integration mit faserbasierten Steuerungs- und Auslesesystemen. Diese Arbeit untersucht die gängigste Methode zur Herstellung von Faserspiegeln für optische Resonatoren. Dabei wird ein Hochleistungs-CO_2-Laser eingesetzt, um durch thermischen Materialabtrag hochwertige Spiegeloberflächen mit anpassbarer Geometrie auf der Faseroberfläche zu erzeugen. Ein Weißlichtinterferometer wird dann zur In-situ-Charakterisierung der hergestellten Strukturen verwendet. Diese Arbeit gibt eine detaillierte Beschreibung des Herstellungsprozesses und untersucht die Auswirkungen verschiedener Produktionsparameter auf Form und Qualität der gefertigten Spiegeloberflächen. Unsere Ergebnisse schaffen die Grundlage für die Fertigung hochwertiger Faserspiegel, die den aktuellen Stand der Technik übertreffen.

Contents

1 Introduction

Fabry-Pérot cavities (FPCs) are a prominent platform for studying atom-light interactions within the scope of cavity quantum-electro-dynamics (CQED). The low photon loss rates and small mode volumes of FPCs enable strong coupling between cavity photons an atoms placed within the resonator field. This provides a powerful framework for performing high-fidelity quantum operations on the coupled atom-light system. In fiber-based FPCs (FFPCs), the resonator mirrors are fabricated directly onto the end faces of optical fibers. One such fiber cavity experiment is currently being built by the Léonard-group. The experiment will use an array of optical tweezers to trap ultra-cold Rubidium-87 atoms in the light field of a FFPC. The interactions between the atoms and the cavity field enable the experimental study of global cavity-mediated interactions between the atoms. Additionally, individual tuning of each atoms coupling strength allows for single atom addressability.

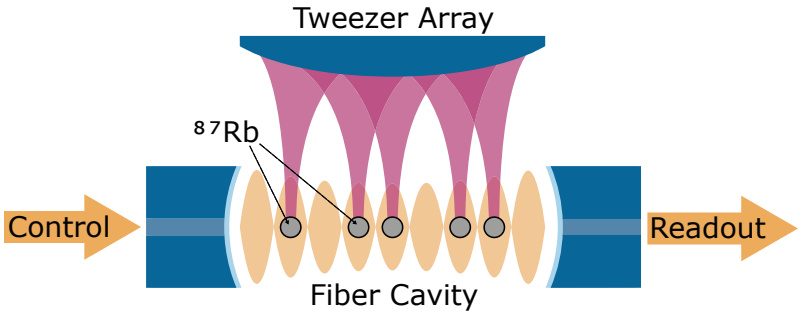

Figure 1.1: Cavity experiment of the Léonard-group. An optical tweezer array captures ^{87}Rb atoms in the light field of a fiber cavity. The cavity field facilitates tunable interactions between the atoms. The optical fibers that function as resonator mirrors also provide integrated control and readout capabilities for the system.

The fiber mirrors we are currently using have a typical radius of curvature of around 150 µm with a spherically curved area of 15 µm diameter. They allow us to construct cavities with a maximum length of about 80 µm and a typical finesse of 30 0000. To reach the goal of eventually fitting up to 100 or more atoms in the cavity and explore a broader range of many-body physics regimes, the length of the resonator will have to be in the order of $100-200$ µm. Achieving these lengths while maintaining strong coupling between the atoms and the light field is not trivial. As the resonator length increases so will the size of the cavity mode and the corresponding mode volume. At some point the cavity mode will extend onto regions of the mirror that do not have a high enough surface quality to support the cavity mode well. This leads to a significant increase of the cavity losses and a corresponding deterioration of the atom-light cooperativity.

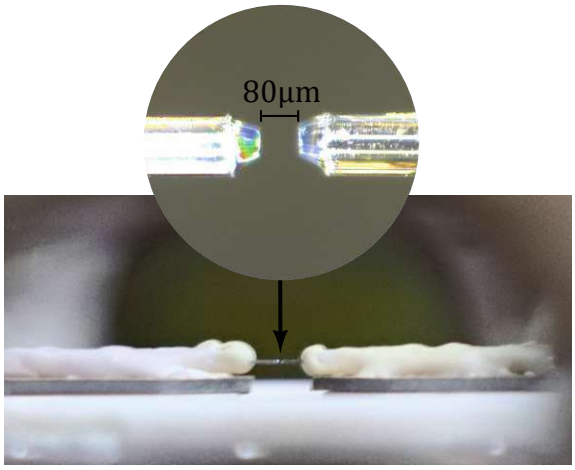

Figure 1.2: Image of the current fiber cavity. The fibers are glued to Piezo-elements to provide active length control. The taper of the fiber ends provides improved optical access.

To further push the capabilities of our fiber cavity experiment and eventually reach the targeted regime of cavity lengths exceeding 100 µm and a finesse upwards of 100 000 we are currently developing our own fiber mirror production setup. The ground work of our current setup was already laid by Isabelle Safa during her internship [17] and Constantin Grave for his master's thesis [4]. The setup uses a high-power CO_2-laser to shape a fiber mirror by ablatively removing material from the end face of an optical fiber. This method of CO_2-laser machining was pioneered by the Reichel-group in 2010 [7] and is by now a well established technique in both scientific and commercial sectors. By tuning various different production parameters such as the beam size of the ablation laser, the laser power during the ablation process or the duration of the ablation pulse one can, in principle, create mirror profiles with an arbitrary and customizable geometry and exceedingly large, high quality mirror surfaces.

This work explores the recent development and refinement of our fiber mirror production process. It describes how the existing ablation setup was expanded and upgraded to facilitate the CO_2-laser-machining of optical fibers. Various techniques for preparation, production and analysis of the fibers were developed to ensure both high quality and reproducibility of the final mirror surfaces. The capabilities of the upgraded ablation setup were demonstrated using the results of various production parameter scans. Finally, the setup was used to produce our first prototype fiber mirrors. These prototypes were already found to be comparable in quality to those of leading research groups.

2 Theoretical Background

2.1 Fabry-Pérot Resonator

2.1.1 Optical Resonator

In its simplest form, a Fabry–Pérot Resonator consists of two parallel reflective surfaces facing each other at a distance L. A light wave coupled into such a cavity repeatedly propagates from one surface to the other where it is reflected back to the first surface. During each of these round trips, the wave accumulates a phase shift of

$$\Delta\varphi = k \cdot 2L = \frac{4\pi\nu L}{c}. \tag{2.1}$$

Here k is the wavenumber and ν is the corresponding frequency.

In the limit of lossless reflectivity ($R = 1$) the wave performs infinitely many of these round trips. The resulting effective field inside the resonator is created by the sum of all individual waves of each respective round trip. If and only if $\Delta\varphi = q \cdot 2\pi$ ($q \in \mathbb{N}$), the wave recreates itself exactly after each round trip. The partial waves then interfere constructively and optical power can build up within the cavity. From equation (2.1) it follows, that the incident wave is on resonance only for discrete and evenly spaced frequencies

$$\nu_q = q \cdot \nu_{\mathrm{FSR}} \qquad \text{where} \qquad \nu_{\mathrm{FSR}} = \frac{c}{2L}. \tag{2.2}$$

ν_q are the resonance frequencies and ν_{FSR} is the so called free spectral range of the cavity.

In any real application, the wave propagating within the resonator experiences absorption and scattering losses as well as transmission losses at the mirror surfaces. During each round trip, the intensity of the wave is reduced by the intensity attenuation factor

$$|r|^2 = R_1 R_2 e^{-2\alpha L} \tag{2.3}$$

where $R_{1/2}$ are the reflectivities of the surfaces and α is the loss coefficient. The losses result in a broadening of the delta-shaped intensity peaks of the cavity spectrum. This is because now destructive interference of the partial waves is no longer perfect and off-resonant waves can also build up finite intensity fields. The spectrum of the resonator field $I(v)$ is described by Airy-shaped functions [18]

$$I(\nu) = \frac{I_{\max}}{1 + (2\mathcal{F}/\pi)^2 \cdot \sin^2(\pi\,\nu/\nu_{\mathrm{FSR}})} \quad \text{with} \quad I_{\max} = \frac{I_0}{(1-|r|)^2} \tag{2.4}$$

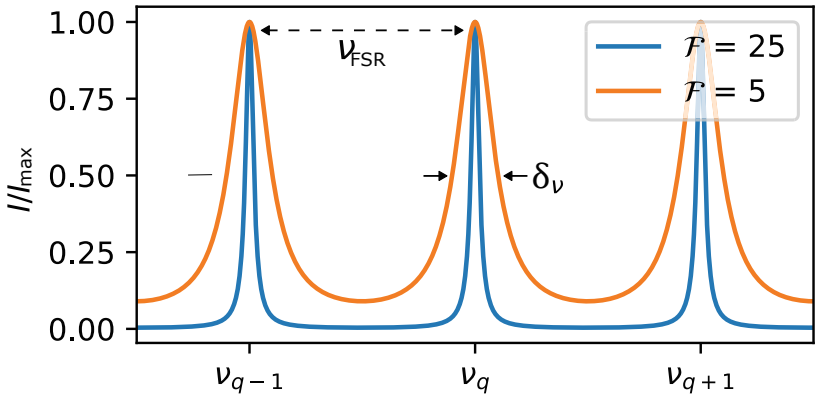

Figure 2.1: The spectrum of a Fabry-Pérot resonator has the form of Airy-peaks centered around the resonance frequencies ν_q. The free spectral range ν_{FSR} is the separation of two peaks. The width δ_v of each peak depends on the finesse $\mathcal{F}$ of the resonator.

with peaks centered around the resonance frequencies ν_q. In the above equation we introduced an important parameter $\mathcal{F}$ called the finesse of the cavity which compactly describes the losses of the resonator and is defined as

$$\mathcal{F} = \frac{\pi\sqrt{|r|}}{1-|r|}. \tag{2.5}$$

The finesse is closely connected to the full width at half maximum (FWHM) of the intensity peaks δ_ν and for $\mathcal{F} \gg 1$:

$$\delta_\nu = \frac{\nu_{\mathrm{FSR}}}{\mathcal{F}}. \tag{2.6}$$

Figure 2.1 shows the typical spectrum of a Fabry-Pérot resonator for different values of $\mathcal{F}$.

Fabry-Pérot Resonator with spherical mirrors

One major problem of using flat surfaces in a Fabry-Pérot cavity is the low confinement of the field within the resonator. Even the smallest misalignment of a mirror leads to the light leaving the cavity. Additionally as the wave propagates between the mirrors it generally broadens, resulting in large mode volumes of the resonator field. Both of these problems can be addressed by using spherical mirrors. The resulting cavity geometry is much less sensitive to misalignment and the spherical shape of the mirrors enforces new boundary conditions on the cavity field. Stable modes of the cavity now take the form of Gaussian beams.

A Gaussian beam is a solution of the paraxial Helmholtz equation. The intensity of such a beam traveling along the z-axis is described by a Gaussian distribution.

$$I(r,z) = I_0\left(\frac{W_0}{W(z)}\right)^2 \exp\left(-\frac{2r^2}{W^2(z)}\right) \tag{2.7}$$

where r is the radial distance from the z-axis and $W(z)$ is the beam radius or beam width. The beam radius is defined as the distance from the z-axis at which the intensity drops by a factor of $1/e^2$. The beam size has its minimum value at the beam waist W_0 which we here assume to be located at $z = 0$. Moving away from the waist along the beam axis, the beam expands according to

$$W(z) = W_0\sqrt{1 + \left(\frac{z}{z_R}\right)^2} \qquad \text{where} \qquad z_R = \frac{\pi W_0^2}{\lambda}. \tag{2.8}$$

z_R is called the Rayleigh-length and is the distance from the waist along the z-axis at which the beam has expanded by a factor of $\sqrt{2}$. The radius of curvature (ROC) of the wavefront of a Gaussian beam is also position dependent and has its minimum at z_R

$$R(z) = z\left[1 + \left(\frac{z_R}{z}\right)^2\right]. \tag{2.9}$$

The exact shape of the Gaussian cavity field is determined by the boundary condition that the ROC of the wavefront matches the ROC at the mirrors. Whether a given mirror geometry can support a stable resonator mode is expressed by the stability criterion [2]:

$$0 \ll \left(1 - \frac{L}{R_1}\right)\left(1 - \frac{L}{R_2}\right) \ll 1 \tag{2.10}$$

where L is the cavity length and R_i are the ROCs of the cavity mirrors. Figure 2.2 depicts various stable cavity geometries.

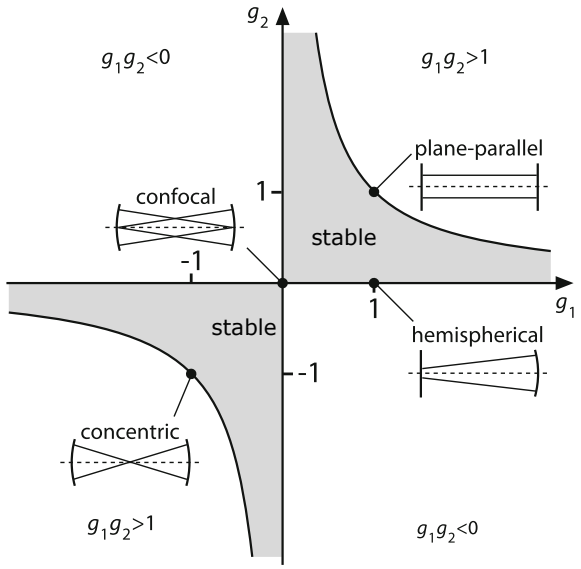

Figure 2.2: Stable configurations of resonators with curved mirror geometries satisfy the stability criterion $0 \ll g_1 g_2 \ll 1$ with $g_i = (1 - L/R_i)$. Figure adapted from [2].

A cavity with spherical mirror geometry does not only support the fundamental Gaussian beam mode (TEM_{00}) but also waves with non-zero transversal modes with

cylindrical symmetry ($\mathrm{TEM}_{l,m}$). They are also solutions to the paraxial Helmholtz equation and therefore have identical wavefronts. The resonance frequencies of the fundamental and higher order modes are shifted with respect to the resonance frequencies ν_q of the plane resonator by corrections that account for the curved mirror geometry and transversal excitations [18]

$$\nu_{q,l,m} = \nu_q + (l + m + 1)\frac{\Delta\varphi}{\pi}\nu_{\mathrm{FSR}} \tag{2.11}$$

with $\Delta\varphi = \varphi(z_2) - \varphi(z_1)$ and $\varphi(z) = \arctan(z/z_r)$ where $z_{1/2}$ are the positions of the mirrors.

As we will see later, the mirror profiles produced via CO_2-laser ablation are not always perfectly spherical and can show some ellipticity. The different radii of curvature along the major and minor axis of such an ellipsoid can cause birefringence to occur within the cavity field. Birefringence is a phenomenon in which the normally degenerate polarization eigenstates of the cavity field split up due to the asymmetrical mirror geometry. The frequency splitting δ_{BF} of the polarization modes aligned with the principal axes of the mirror surface can be calculated as [21]

$$\delta_{BF} = \frac{\nu_{\mathrm{FSR}}}{2\pi k}\frac{R_a - R_b}{R_a R_b} \tag{2.12}$$

with $R_{a/b}$ being the radii of curvature of the respective axis. Generally birefringence is not desired in cold atom cavity experiments as it can decrease the coupling strength between atoms and the cavity photons. Furthermore precise control of photon polarization is often essential for many different quantum (readout) protocols.

2.1.2 Cavity QED

To better understand how cavity geometry and finesse influence the interactions of atoms and the resonant light field we consider the simplest case of a single atom placed inside a cavity. The resonance frequency ω_c of the cavity is tuned close to the atomic transition frequency ω_a between the ground state $|c\rangle$ of the atom to some excited state $|e\rangle$ (see Fig. 2.3b). The dynamics of such a system can be described with the Jaynes-Cummings Hamiltonian:

$$\mathcal{H} = \hbar\omega_a\hat{\sigma}^\dagger\hat{\sigma} + \hbar\omega_c\hat{a}^\dagger\hat{a} + \hbar g(\hat{\sigma}^\dagger\hat{a} + \hat{\sigma}\hat{a}^\dagger) \tag{2.13}$$

Here the first two terms describe the energies of the isolated atom and the empty cavity respectively. $\hat{\sigma}^\dagger/\hat{\sigma}$ are the creation/annihilation operators for the excited atom state and $\hat{a}^\dagger/\hat{a}$ are the creation/annihilation operators for a photon in the cavity. The last term in Eq. (2.13) describes the interactions between cavity photons and the atom. Specifically, they express the excitation of the atom through absorption of a photon ($\hat{\sigma}^\dagger\hat{a}$) and the decay of the excited atom ans subsequent release of a photon into the cavity mode ($\hat{\sigma}\hat{a}^\dagger$). The coherent coupling rate g describes the effective strength of these dipolar interactions and can be calculated as [16]

$$g = g_0 u(\vec{x}) \qquad \text{with} \qquad g_0 = d\sqrt{\frac{\omega_c}{2\hbar\varepsilon_0 V_m}}. \tag{2.14}$$

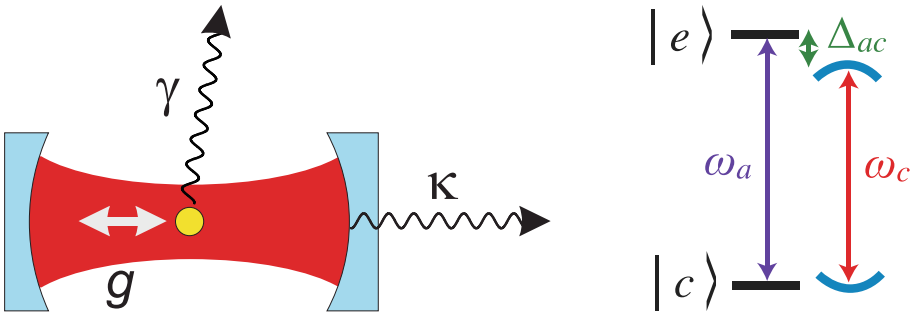

(a) (b)

Figure 2.3: (a) A single atom placed inside a cavity interacts with the cavity photons with the coupling rate g. κ is the photon loss rate of the cavity and γ is the decay rate of the atom into free space. Figure adapted from [8]. (b) Two level atom with the coupled ground state $|c\rangle$ and an excited state $|e\rangle$. The cavity (ω_c) is close to resonance with the atomic transition frequency ω_a with a detuning of Δ_{ac}. Figure adapted from [16]

Here, $u(\vec{x})$ is a dimensionless function describing the spatial distribution of the electric-field mode. It is typically normalized to a value of 1 at the location of maximum field strength, usually at the position of the beam waist. g_0 is the coupling rate at the field maximum with the atomic dipole moment d and the mode volume V_m. The mode volume is defined as the integral over the mode function $V_m = \int |u(\vec{x})|^2 d^3x$. For short cavities with $L \lesssim 2z_r$, the divergence of the electric field is small enough that we can approximate $g \simeq g_0$ and $V_m = \frac{\pi}{4} W_0^2 L$.

In order to perform quantum operations with high fidelity, one typically needs to be in the strong coupling regime where the coherent interaction rate g is large compared to the rate of incoherent losses of the system. We can differentiate between two different loss processes (see Fig. 2.3a). κ is the decay rate of photons leaving the cavity either via scattering, absorption or transmission at the resonator mirrors. It can directly be related to the cavity finesse:

$$\kappa = \frac{\pi c}{2L\mathcal{F}}. \tag{2.15}$$

γ describes the photon loss when the excited atom decays and the resulting photon is released into free space rather than the cavity field. To achieve strong coupling g needs to be large with respect to both κ and γ. We can express this requirement with the single atom cooperativity C:

$$C = \frac{g^2}{2\kappa\gamma} \gg 1 \tag{2.16}$$

In order to achieve high single atom cooperativities in the order of $C \sim 100$ one needs to both increase the coherent coupling g and decrease the incoherent losses κ as much as possible. To increase g we use tightly confined cavity fields with small beam waists W_0 and small mode volumes V_m. To decrease κ, the finesse $\mathcal{F}$ of the cavity should be as high as possible.

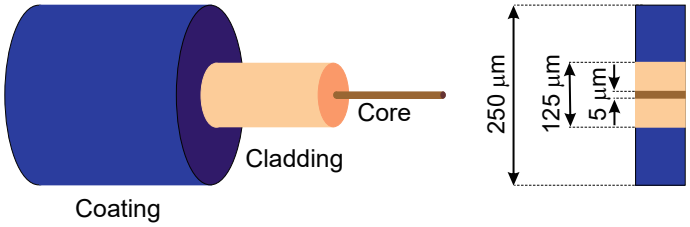

Figure 2.4: Sketch of the layer structure of an optical fiber. The electromagnetic wave is guided within the fiber core. The coating protects the fiber and gives mechanical stability. The dimensions shown are typical diameters for standard single-mode fibers. Figure taken from [19].

2.2 Fiber Fabry-Pérot Cavities

2.2.1 Optical Fibers

Optical fibers are dielectric waveguides widely used in telecommunications and optical technologies for their ability to transmit electromagnetic waves coherently and with minimal loss over large distances. Fused silica (SiO_2) is typically used as the bulk material of the fiber. Figure 2.4 shows the typical layer structure of an optical fiber. The center region (core) is usually doped with materials such as germanium or fluorine to change its refractive index with respect to the surrounding silica layer (cladding). The outermost layer of the fiber (coating) provides mechanical stability and protection against damage. Various materials ranging from different polymer compounds to metals such as aluminum of copper are used to coat fibers.

The distribution of the doping materials determines the refractive index of the core and in extension the optical properties of the fiber as shown in Figure 2.5. Small fiber cores only accept a single optical mode, the fundamental TEM_{00} mode, while larger doped cores also enable different higher order modes to propagate through the fiber. In step-index fibers, core and cladding each have a constant refractive index with a step at the boundary between the regions. If the angle of a ray traveling in the fiber is shallow enough, total reflection at the boundary between core and cladding keeps the light contained within the core. Graded-index fibers (GRIN) are doped in a way that the refractive index is maximal at the center of the core and decreases towards the cladding. In these fibers the light rays are bent towards the center of the fiber due to the gradient of the refractive index. The advantage of GRIN doping is that it mitigates modal dispersion which is typically encountered in conventional step-index multi-mode fibers.

2.2.2 Fiber Fabry-Pérot Cavities

In a fiber Fabry-Pérot cavity (FFPC), the end faces of two optical fibers are used as mirror surfaces as shown in figure 2.6. Even though their finesse is generally lower compared to high finesse cavities using macroscopic superpolished mirrors, FFPCs still present a compelling choice for atom-light coupling CQED experiments for a few different reasons.

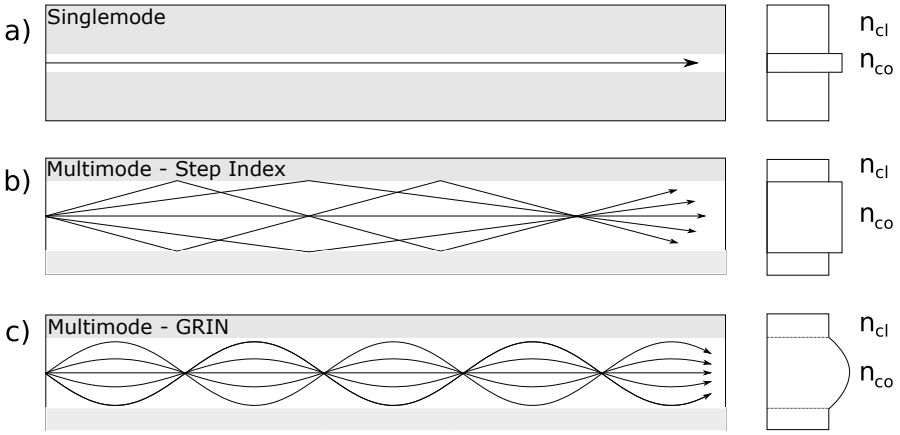

Figure 2.5: The cross section of the refractive index of a fiber (shown on the right) determines the properties of the fiber. Single-mode fibers a) have a small core and only accept the fundamental optical mode. Step index multi-mode fibers b) and GRIN multi-mode fibers c) have larger cores allowing different modes to propagate within the fiber. Figure adapted from [13]

The small form factor of fiber-based cavities generates light fields with small beam sizes of typically only a few micrometers. As detailed in section 2.1.2 the resulting small mode volume V_m leads to an increased coupling rate g and a higher cooperativity C between the atoms and the light field. An additional benefit of the compact geometry is the enhanced optical access it provides to other parts of the experiment, such as imaging beams or atomic tweezers.

Another major advantage of FFPCs is the inherent coupling between the cavity field and the optical fibers. This enables easy active stabilization, probing and readout of the cavity system via the cavity fibers. A common combination of fibers, also used in our cavity experiment, uses a single-mode fiber to couple a locking signal as well as the probing beam into the cavity. A multi-mode fiber is used to collect the photons used for cavity readout. The efficiency with which light couples into or out of the cavity depends largely on the overlap or mode matching between the fiber and the resonator modes. For perfect collinear alignment, the mode matching efficiency can be calculated as [6]

$$\epsilon = \frac{4}{\left(\frac{W_f}{W_m} + \frac{W_m}{W_f}\right)^2 + \left(\frac{\pi n W_f W_M}{\lambda R}\right)^2} \tag{2.17}$$

where $W_{f/m}$ are the beam sizes of fiber/cavity mode, n is the refractive index of the fiber and R is the radius of curvature of the mirror surface. Any form of translational or angular misalignment of the fibers lead to a, potentially significant, decrease in coupling efficiency.

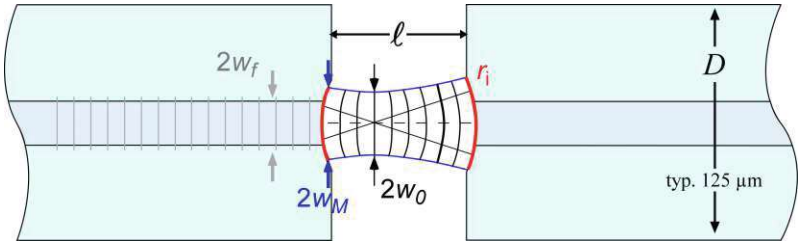

Figure 2.6: Sketch of a fiber Fabry-Pérot cavity. The coupling efficiency is determined by the mode matching of the cavity mode and the fiber mode. Figure adapted from [15].

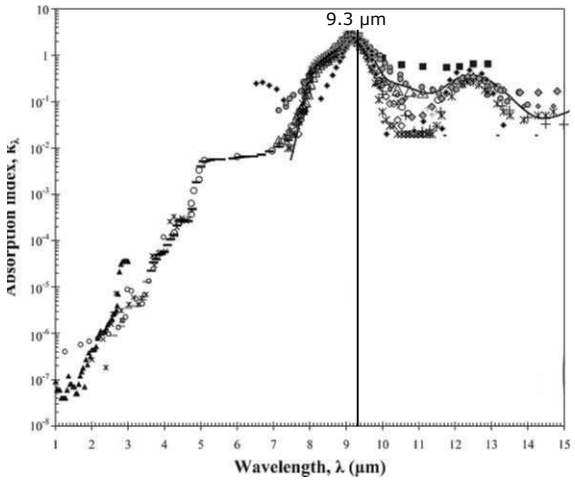

Figure 2.7: Absorption spectrum of fused silica (SiO_2) with maximal absorption at 9.2µm. The wavelength of the CO_2-laser we are using has a wavelength of 9.3 µm close to this absorption maximum. Figure adapted from [12].

2.3 Mirror Shaping using CO_2-laser Ablation

2.3.1 CO_2-laser Ablation

As outlined in previous sections, high quality mirror surfaces are crucial for CQED experiments as even the smallest imperfections introduce additional losses that can quickly deteriorate atom-light cooperativity.

To create the desired mirror profile on a glass plate or the end face of a fiber, the designated surface is illuminated with a high power laser beam. The substrate absorbs the incoming light and heat up in the process. As the temperature rises, the material first liquefies before starting to evaporate at temperatures above $\sim 2000°C$. Figure 2.7 shows the absorption spectrum of fused silica which has an absorption maximum at 9.2µm. The laser we are using has a wavelength of 9.3µm which lies close to that maximum. This means that the laser light does not propagate too deep within the material and the heating effect is contained to a very narrow region around the surface. This in turn provides precise control of the energy deposition in the material during the ablation process [7].

The local surface temperature during the ablation process depends mainly on the intensity profile of the incident beam $I(r)$, which generally follows the Gaussian

distribution of Eq. (2.7). One can solve a two dimensional heat-flow equation to calculate the temperature distribution $T(r,t)$ on the substrate surface [3]

$$T(r,t) = \frac{AW^2}{\kappa}\sqrt{\frac{D}{\pi}}\int_0^t \mathrm{d}\tau \frac{I_0(t-\tau)}{\sqrt{\tau}(W^2+4D\tau)} e^{-\frac{r^2}{W^2+4D\tau}} \tag{2.18}$$

where A is the absorption coefficient, D is the thermal diffusivity and κ is the thermal conductivity of the material. W is the beam size and $I_0(t)$ is the intensity at the center of the laser beam. The rate at which material is evaporated $v(r,t)$ depends strongly on the local temperature $T(r,t)$ [7]:

$$v(r,t) = v_0 \exp\left(-\frac{U}{k_B T(r,t)}\right) \tag{2.19}$$

Here $v_0 = 3.8 \cdot 10^{-5}$cm/s is a constant velocity of evaporation and $U = 3.6$ eV is the latent heat of the evaporation of a single atom. The predicted profile produced during the ablation process is approximately Gaussian with a radial depth profile of

$$z(r) = z_0 \exp\left(-\frac{U}{k_b T(0,\tau)}\frac{r^2}{2W^2}\right) \equiv z_0 \exp\left(-\frac{r^2}{\rho^2}\right) \tag{2.20}$$

where $T(0,\tau)$ is the temperature of the center point after a laser pulse of length τ. $\rho \equiv W\,(2k_b T(0,\tau)/U)^{1/2}$ is the $1/e$ radius of the Gaussian profile. The model above describes a very idealized scenario of an infinitely large surface. Potentially significant, processes like cooling due to evaporation, flow of liquid material due to surface tension or other non-linear thermal effects are also negleted. Nevertheless, results of other groups show, that the profiles generated through CO_2-laser ablation consistently exhibit the Gaussian shape predicted by the model [7, 20]. In particular, short laser pulses lasting up to a few milliseconds are well described by the theory. For longer pulses with higher power, non-linear processes seem to become increasingly significant and deviations from the Gaussian profile become more prominent.

2.3.2 Geometric Considerations

As outlined in the previous section, the structures created via CO_2-laser ablation generally shows a Gaussian depth profile. However, we ideally would like the profiles to be as spherical as possible to ensure proper mode matching between the cavity mode and the mirror surface. To estimate the "spherical-ness" of the produced profiles we can use the quadratic term of the polynomial expansion of the Gaussian in eq. (2.20) as an approximation for an exact circular profile with radius R.

$$z(r) \cong z_0\left[1 - \frac{r^2}{\rho^2} + \mathcal{O}(r^4)\right] \tag{2.21}$$

As we see from Figure 2.8 this approximation is very accurate for $r \ll R$. The radius of curvature R_0 at the center of the Gaussian is calculated as

$$R_0 = \left|\frac{(1+z'^2)^{3/2}}{z''}\right|_{r=0} = \left|\frac{\rho^2}{2z_0}\right| \tag{2.22}$$

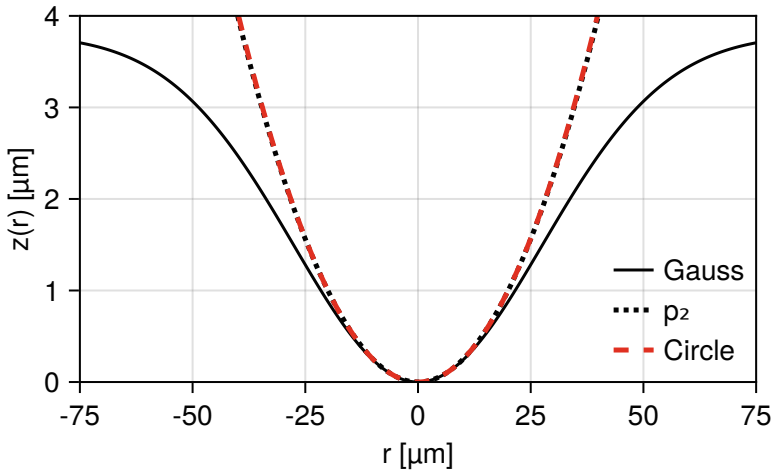

Figure 2.8: Ideal Gaussian profile with typical parameters of R = 200 µm, $z_0 = 3.8$ µm and $\rho = 39$ µm. The quadratic term of the Gaussian function (p_2) is a good approximation for a spherical profile for $r \ll R$.

From this relation we see that the structure depth z_0, width ρ and the ROC at the center are not independent of one another. This means that by fixing two of those quantities the third is uniquely determined. By tuning the laser parameters during the fabrication process we can access different parameter regimes. Large beam sizes produce broader and shallower holes with large ROCs while increasing the laser power or pulse duration result in deeper holes with small ROCs. Finding the right laser parameters for the ablation process is one of the key challenges in the development of the fiber ablation setup.

3 Experimental Setup

This chapter will give an overview of the fiber production setup used throughout this work. It will also describe the methods used for the characterization of different components and the reconstruction algorithm used for the reconstruction of the observed surface profiles.

Figure 3.1 shows a schematic of the whole fabrication setup. The CO_2-laser setup (3.1a) is used during the ablation process itself. It includes the high power CO_2-laser as well as all the optics required to align, shape and focus the beam onto the fiber tip. The imaging setup (3.1b) is used for both positioning the fiber as well as analyzing the surface profile before and after the ablation process. For this purpose we employ white-light interferometry using a light source with a broad spectrum in combination with a Mirau objective. The short coherence length of the imaging light enables extremely precise surface reconstruction with an accuracy down to the nanometer scale.

The fibers themselves are mounted on high-precision 3-Axis translations stages[1] to move between both parts of the setup. A power meter[2] is installed behind the ablation area to monitor beam power and characterize the laser beam via the knife edge method. All devices of the setup are operated via a connected PC using a custom LabView based control program.

3.1 CO2-laser Setup

In the laser ablation setup a liquid-cooled CO_2-laser[3] is used. The laser has a nominal wavelength of 9.3µm and a rated optical power output of 40 W. The actual power output of the laser is significantly higher and was measured to be about 55 W. Both the high power and the mid-infrared wavelength pose a significant challenge when working with the laser. Conventional optical elements, like SiO_2 lenses and mirrors, are unsuitable at the required regimes. Therefore, more unconventional materials like ZnSe-lenses and gold-coated metal mirrors have to be used in the optical setup for the laser.

[1] Newport XML210-S, XMS50-S and MLT25-Z
[2] Coherent PowerMax 150
[3] Coherent DIAMOND C-55

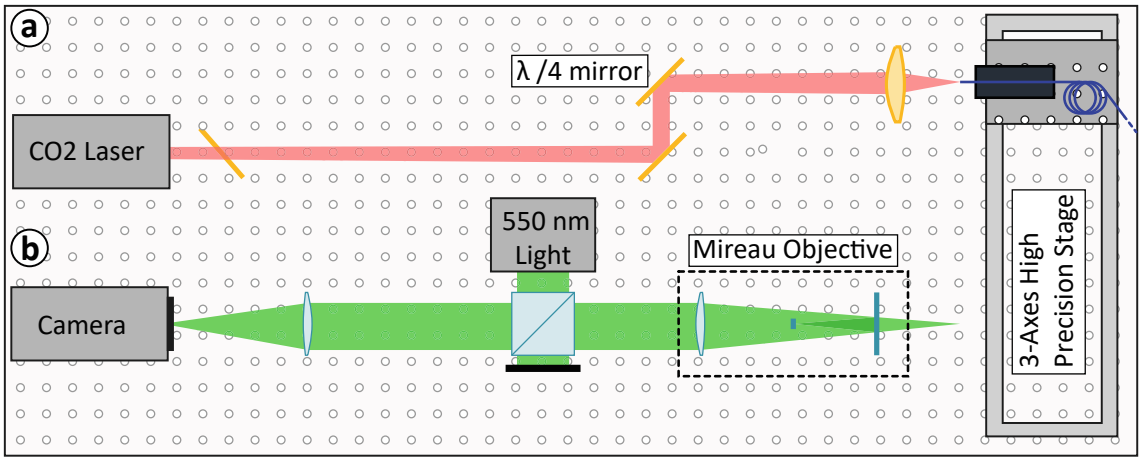

Figure 3.1: Schematic of the fiber production setup. A CO_2-laser generated the ablation light which is then focused onto the fiber tip. (b) The fiber surface is analyzed using a white-light interferometer consisting of a broadband light source and a Mirau-objective. A high precision 3-axis translation stage is used to accurately position the fibers during the production process.

Laser Polarization

The light emitted from the laser has a linear polarization. Other groups using CO_2-machining observed an increased ellipticity in the produced structures when using linearly polarized light compared to a circular polarization [21]. We therefore also polarize our beam circularly by using a phase shifting mirror (PSM). By reflecting the beam at an angle of 45° with respect to the polarization axis we induce a phase shift of $\pi/2$ to one of the diagonal polarization modes resulting in the desired circular polarization. Figure 3.2 shows an image of our laser setup and depicts the 45° reflection using a PSM.

3.1.1 Laser Pulses

The laser model we are using cannot output arbitrary power in a continuous wave (CW) mode but instead outputs light only at the maximum optical power of 55 W. To tune the effective (average) power, one has to use pulse width modulation (PWM) in which the laser is continuously turned on and off by applying a periodic rectangular signal to the corresponding control pin of the laser (see Figure 3.3). The duty cycle is the percentage of the total period during which the laser outputs power. It is thus roughly equivalent to ratio of average to maximum output power.

During testing of the ablation setup it became apparent that single laser pulses of only around 50 s were already depositing too much energy into the substrate resulting in cracks, droplets of molten material and other visible defects forming on the ablated surface (see Fig. 4.6c). Since the PWM mode of the laser is not capable of operating at such short timescales, the pulses used during the ablation process were created digitally with a defined pulse length and time separation. Because only a

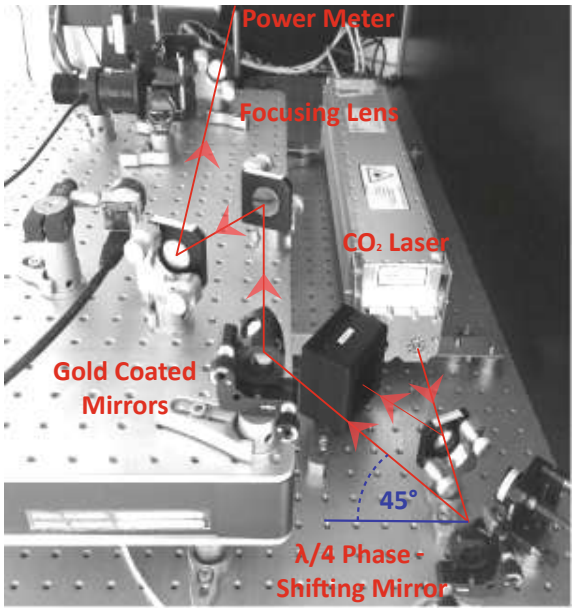

Figure 3.2: Image of the CO_2-laser ablation setup. The initially linearly polarized beam is reflected by a $\lambda/4$ phase-shifting mirror at an angle of 45° to circularly polarize the ablation light. Figure adapted from [4].

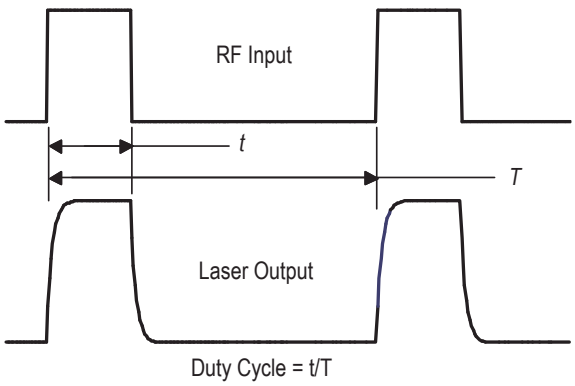

Figure 3.3: Signal and corresponding laser output in PWM mode according to laser manual. The duty cycle t/T (in %) determines the average optical output power of the CO_2-laser. Figure adapted from [1]

.

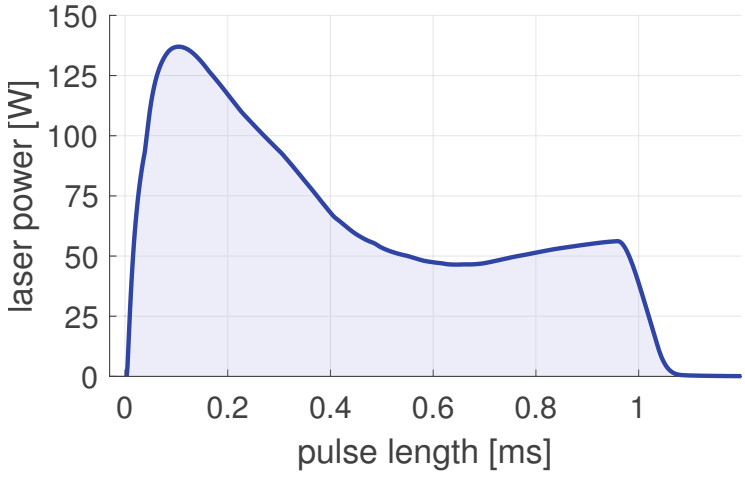

Figure 3.4: Intensity of laser pulses show clear overshoot on the rising edge with power spiking up to 140 W. Only after $\sim$ 500 µs does the laserpower stabilize at the expecte 55 W.

single (or very few) pulses lasting between 5 µs and 45 µs were sufficient for creating the desired structures, the precise intensity profile over time of each pulse becomes much more significant.

To characterize the intensity profile of single laser pulses we use a *Coherent PowerMax-Pro 150 HD* thermal power meter. Figure 3.4 shows the measured intensity over the duration of the laser pulse. We observe a significant overshoot in power up to a maximum of about 140 W at the rising edge of the pulse. Only after about 500 µs does the measured power stabilize at the expected 55 W. Since the observed overshoot happens at a time scale much larger than the specified reaction time of the power meter ($<$ 10 µs) the overshoot is most likely caused by the laser itself. The typical pulse length falls right within the steep slope of the rising edge of the pulse. This means that the total energy deposition during each pulse is highly non-linear with respect to the pulse length.

3.1.2 Beam Characterization

As mentioned in section 2.3, the beam size of the ablation laser must match the dimensions of the structures intended for fabrication. To create mirror profiles with ROCs of a few hundred micrometers, the beam also has to have a waist in the order of $\sim$ 100 µm. To shape the beam accordingly, the natural expansion of the beam over a distance of $\sim$ 1 m is used in combination with a focusing lens with a focal length of $f = 100$ mm (see Figure 3.2). During the fabrication process the fiber is then placed close to the focal point of the beam.

To characterize the exact beam shape close to the beam waist the knife edge method is used. For this, a sharp edge is slowly moved perpendicular to the beam propagation axis blocking an increasing part of light from the beam. During this scan, the unblocked intensity behind the knife is measured as a function of the edge

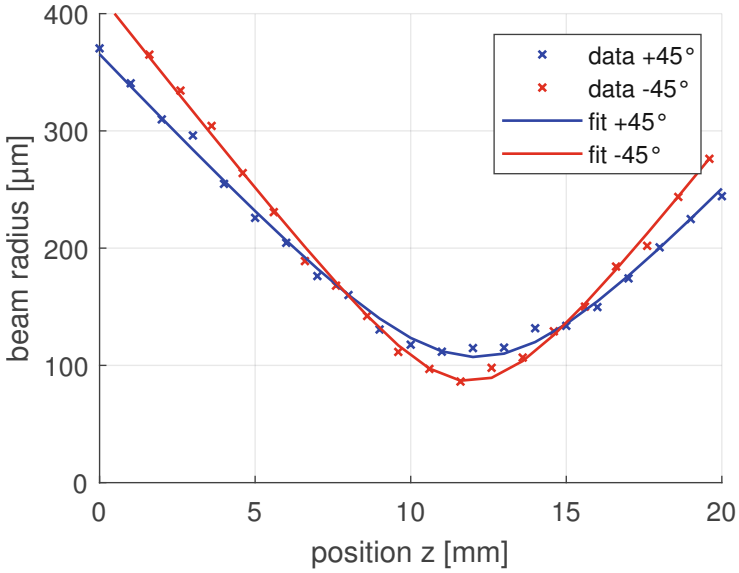

Figure 3.5: The beam profile of the ablation laser measured via the knife edge method shows clear ellipticity along the ±45° degree axes. A fit with the Gaussian beam expansion yields beam waists of $W_0^{+45} = 107\,\mu\text{m}$ and $W_0^{-45} = 86\,\mu\text{m}$.

position. It has the shape of a Gaussian error function from which the beam size can then be extracted.

At first the beam profile was only measured along the horizontal and vertical directions and no significant ellipticity in the beam profile was observed. However, the first produced mirror profiles showed elliptical asymmetry with a preference along the ±45° axes. The beam characterization was therefore performed again, this time along the diagonal axes of the beam. Figure 3.5 shows the result of the knife edge test along the ±45° axes of the beam. The beam radius was measured at different positions along the beam axis (z) and the results were fitted with the formula of Gaussian beam expansion (Eq. 2.8). The result indeed shows clear asymmetry between the two diagonal axes. The beam waists extracted from the fits are $W_0^{+45} = 107\,\mu\text{m}$ and $W_0^{-45} = 86\,\mu\text{m}$ with Rayleigh lengths of $z_r^{+45} = 3.7\,\text{mm}$ and $z_r^{-45} = 2.5\,\text{mm}$ respectively. A slight astigmatism of $\Delta z_0^{\pm 45} = 0.2\,\text{mm}$ is also observed.

Improper alignment of the focusing lens alone cannot explain the ellipticity observed in Figure 3.5 as the beam sizes along the two diagonal axes diverge when we move closer to the lens (towards small z). This indicates that the asymmetry has to be present even before the beam hits the focusing lens. To verify this the beam shape was measured again with all optical elements removed except for the planar mirrors required to guide the beam to the scanning area. The beam size of the unmodified beam was measured along both the horizontal and vertical as well as the two diagonal axes. The results of this measurement are shown in Figure 3.6.

As expected, there is a significant difference of 1.0 mm in the beam sizes when

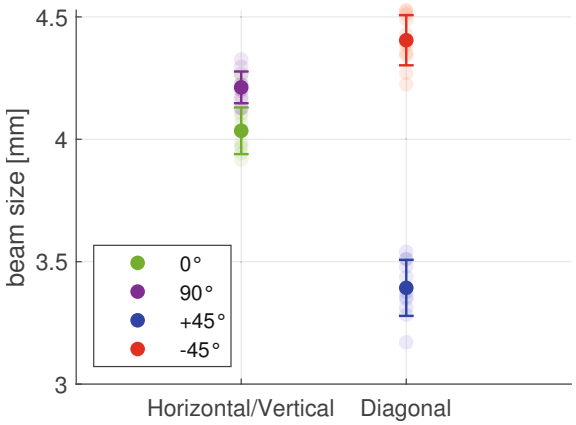

Figure 3.6: Average beam sizes of the unmodified beam measured along different directions at a distance of approximately 1 m. The opaque markers indicate the underlying data points (N=11), the error bars indicate one standard deviation. The beam shows only little ellipticity when measured along the horizontal (0°) and horizontal (90°) axes. When measured along axes rotated by ±45° significant ellipticity is observed.

measured along the ±45° axes. A much smaller difference of only 0.2 mm is measured between the vertical and horizontal directions. This poses some major limitations on the possible shooting parameters since in order to produce symmetric profiles with low ellipticity we cannot shoot at any position along the beam but have to constrain the shooting position to be close to the crossover of the two beam radii ($z \approx 7 - 8\,\text{mm}$ in Figure 3.5).

3.2 Imaging Setup

The imaging setup is the second central system of the production setup. It provides two essential functionalities. Firstly it serves as the main point of reference for positioning the fiber during the fabrication process. Secondly it enables the analysis of the fiber surface before and after the ablation process by utilizing white light interferometry.

3.2.1 White Light Interferometer

Figure 3.1b shows a schematic of the imaging setup. A light source[4] with a central wavelength of $\sim 550\,\text{nm}$ and a spectral width of $\sim 100\,\text{nm}$ is used to illuminate the object. A Mirau-objective[5] focuses the light onto the fiber-surface. A CMOS camera[6] is used in combination with a focusing lens ($f = 200\,\text{mm}$) to capture the image from the objective. Figure 3.7 shows the working principle of a Mirau-objective. Inside the objective, a semi-transparent mirror separates a portion of the light creating the two beam paths of the interferometer. After internal reflection the separated

[4] Thorlabs MINTL5
[5] Nikon CF IC EPI PLAN DI 20X
[6] Alvium 1800 U-319

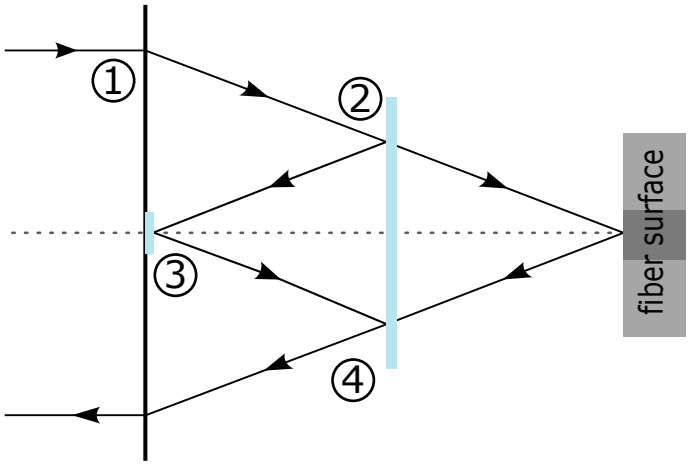

Figure 3.7: Working principle of a Mirau-objective. The incoming light is focused onto the fiber tip by the objective lens (1). A part of the light is split off with internal beam splitter (2). The seperated light is internally reflected (3) before being recombined with the light scattered off the surface (4).

beam is combined once again with the light scattered off the imaged object. The broad spectrum of the white light source results in a very short coherence length ($\sim 1\,\mu m$) of the imaging light. Interference between the two beam paths can thus only occur when the distance to and from the object is precisely the same as the path length of the internally reflected beam. Figure 3.8b) shows the measured intensity of a single pixel as a function of the distance between object and objective. The characteristic oscillations in intensity resulting from interference of the two beams paths are enveloped by a Gaussian function as a result of the short coherence length of the imaging light. Figure 3.8a shows the typical interference patterns created through uneven heights in the surface profile of a fiber. Regions with broad stripes indicate flat profiles with small height variations while areas with narrow stripes result from steep surface gradients.

3.2.2 Surface Reconstruction

To reconstruct a precise 3D-profile of the observed surface the distance between the object and the objective is scanned in small steps of typically 10 nm. After each step the interference pattern on the camera is recorded. Depending on the total height variation of the observed surface, the scanning process usually requires between around 300 and 1000 steps covering a total distance of $3\,\mu m - 10\,\mu m$. After the scan is completed the intensity profile of each pixel as shown in Figure 3.8b is extracted from the recorded images. If two pixels have a height difference of dz between them, the maximum of their respective envelope functions shifts by the same amount relative to each other. In addition to that, there is also a relative phase shift of

$$d\varphi = \frac{dz}{(\lambda_{\text{eff}}/2)} \cdot 2\pi \tag{3.1}$$

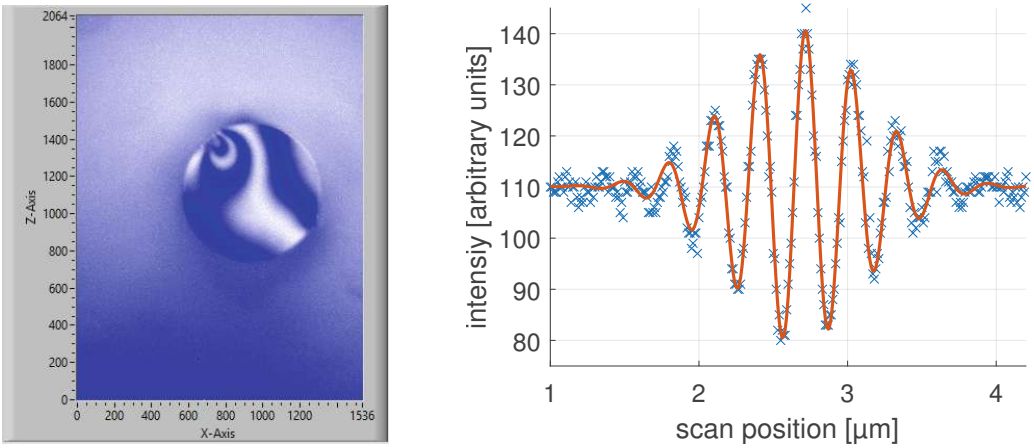

(a) (b)

Figure 3.8: (a) Interference patterns on the fiber surface as seen in the control program. (b) Intensity of a single pixels oscillates with the distance between objective and surface. The plot shows the data points (blue) as well as a fit with a sinusoidal function with a Gaussian envelope (red).

between the sinusoidal parts of the intensity profiles. Here $\lambda_{\text{eff}} \cong 600\,\text{nm}$ is the effective wavelength of the imaging light used in our setup. From equation (3.1) we see that by determining the relative phase differences between all pixels we directly gain information about the height profile of the analyzed surface.

The profile reconstruction is performed in three consecutive steps. First the intensity profiles are fit with the Gaussian enveloped sinusoidal function shown in figure 3.8b. Since this fit has to optimize multiple parameters simultaneously (i.e. amplitude, frequency, offset etc.), it would be a considerable computational effort to fit each individual profile with this exact function. Therefore the exact fit is only performed on a small subset of 5000 profiles and an average of all fitting parameters, except for the phase, is calculated. In a second step each intensity profile is then fit with a pure sinusoidal with the averaged amplitude and frequency determined in the previous step (see Fig. 3.9). Since this fit only requires optimization of the phase it is much faster than the exact fit with multiple parameters. The result of the second fit is a phase map which encodes the relative phase differences between all pixels. In a third step this phase map is then unwrapped to create the final 3D surface profile as shown in figure 3.10. For the unwrapping process a MATLAB implementation [11] of the algorithm developed by Herráez et al. [5] is used.

The phase unwrapping method presented above generally works well for reconstructing the profiles of smooth and continuous surfaces with precision at the namometer scale. The presence of defects such as cracks or very steep gradients on the analyzed surfaces may result in significant noise in the phase map as shown in figure 3.11. If the noise level of the phase map becomes too large, the unwrapping algorithm may start to fail leading to discontinuities in the affected regions.

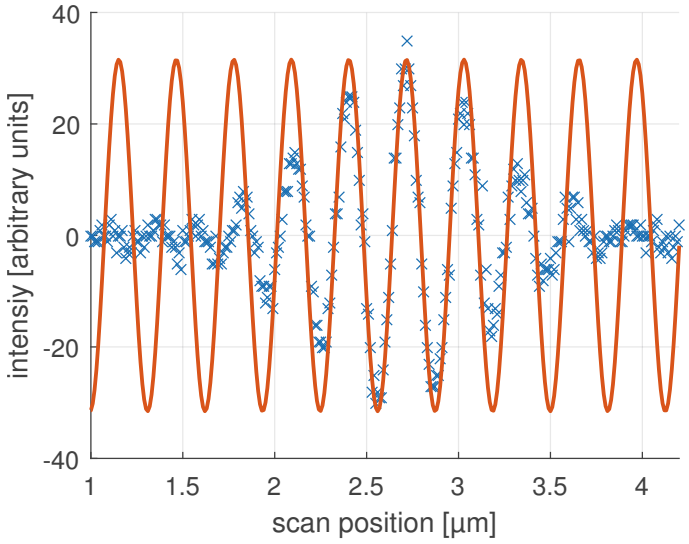

Figure 3.9: To reconstruct the complete 3D surface, the intensity profile of each pixel is fit to extract the relative phase information required in the phase unwrapping process. To reduce computation time of the phase fitting process each intensity profile is fit with a pure sinusoidal. Amplitude and frequency of the fitting function are averaged from exact fits on a subset of all intensity profiles.

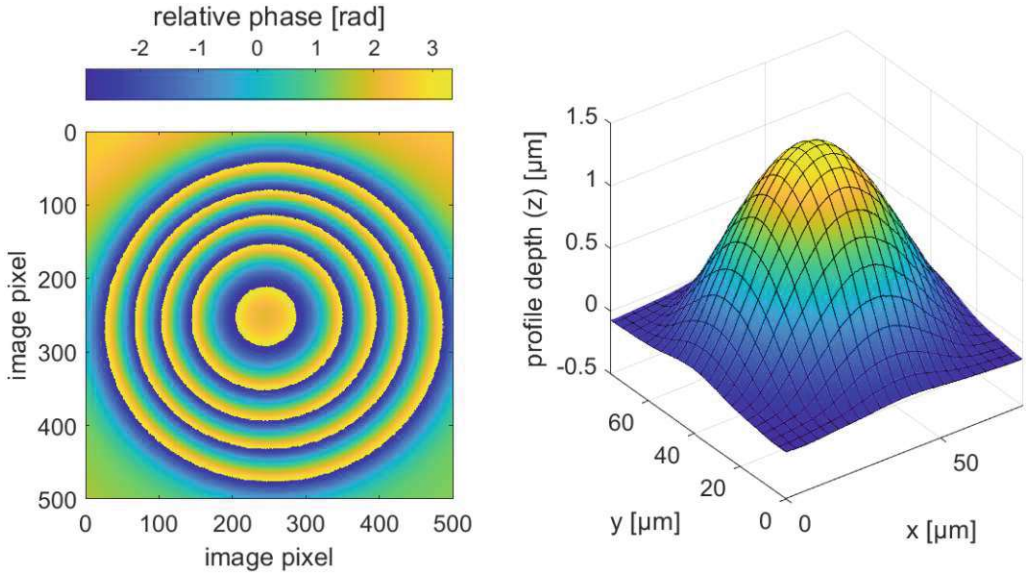

Figure 3.10: With the phase information acquired in the previous fitting routine, the complete 3D surface is reconstructed from the phase map via a phase unwrapping algorithm.

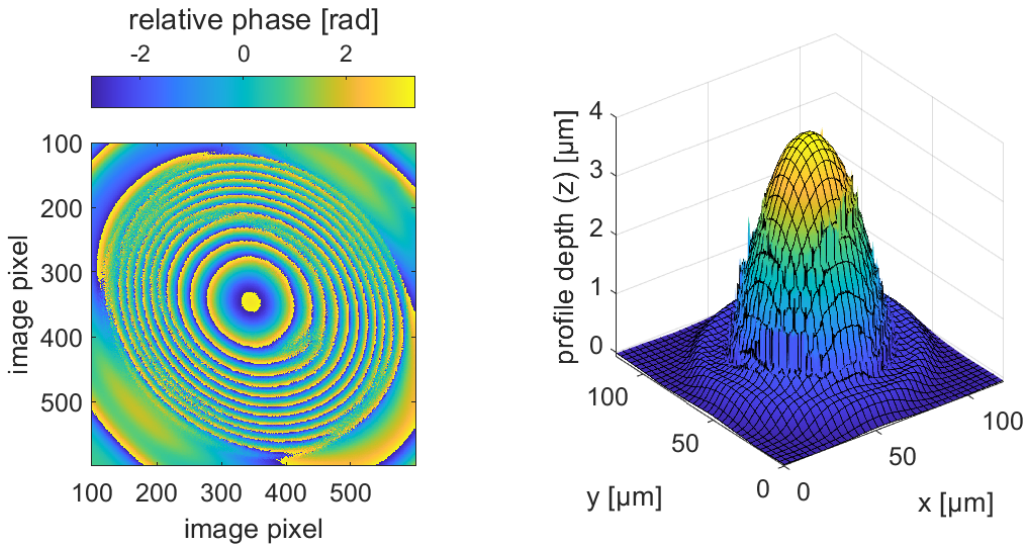

Figure 3.11: (a) Large noise in the phase map may either be caused by surface defects such as cracks and sharp edges or by steep surface gradients resulting in a blurring of the interference pattern. (b) The phase unwrapping algorithm can struggle to accurately reconstruct the profile in regions of high phase noise leading to discontinuities and other artifacts on the reconstructed surface.

4 Fiber Production Process

This chapter will give a detailed description of the whole fiber production process using the previously introduced setup. The production process starts with the preparation of the optical fibers for the the ablation process and ends with the characterization of the final machined mirror profiles.

4.1 Preparation of Fibers

Before the actual ablation process can begin, the fibers have to be prepared carefully to ensure a consistent and precise end result. This preparation process includes stripping the fiber of its protective coating and carefully cleaving the fiber to produce a high quality end face on which the mirror profile can be formed.

4.1.1 Fiber Stripping

The first step in the fiber production process is to remove the coating layer of the fiber also called “stripping". This is necessary to ensure a successful cleaving of the fiber. Various materials like different polymers or metals are used to coat optical fibers. The fiber models we are using[1] are coated with a $\sim 150\,\mu m$ thick layer of polyimide. The polyimide bonds well to the inner layers and provides excellent mechanical stability to the fiber. More importantly polyimide coated fibers are compatible with ultra-high vacuum (UHV) environments, which is essential for the intended use in main cavity experiment. In contrast to metal-coated fibers, which are also used in UHV applications, polyimide is also non corrosive. There are three common methods for stripping polyimide coated fibers.

- **Mechanical stripping:** In the mechanical stripping process, sharp knife edges are used to scrape off the polyimide from the underlying cladding layer. Imprecise mechanical stripping of the fiber may cause chipping of the cladding layer reducing both its mechanical and optical quality. In addition, commercially available high precision mechanical fiber stripper are generally expensive.
- **Chemichal stripping:** For chemical stripping the fibers are treated with hot and aggressive acids such as sulfuric acid to remove the coating. While this process is generally gentle to the inner fiber layers, safe handling and disposal of the involved chemicals can prove difficult.
- **Heat stripping:** Heat stripping involves heating the coating layer and burning away the polyimide. This is the easiest of the three methods as it generally

[1] SM: iXBlue IXF-SRAD-SM-800-014-PI; MM: AMS Technologies MPN:FIP050125145

can be done without the need for expensive equipment. However, overheating or melting of the inner fiber layers can also deteriorate mechanical stability and optical quality of the fiber.

From those three methods heat stripping was chosen for this work as it is quick and no resource-intensive setup is required. To strip the fibers, they are first mounted in a "fiber holder" (Fig. 4.1a). The fiber ends are then heated carefully with a gas torch until no visible coating remaines on the fiber. The stripped fibers are then wiped clean with an optical tissue soaked in ethanol or isopropanol to remove any remaining burnt residue. Aluminum foil is used to cover the unstriped part of the fiber during the stripping process to reduce the size of the burnt residue at the crossover of the stripped and unstripped sections (see Fig.4.1b). If too much heat is applied during the stripping process the fibers will get damaged, typically in the form of melting and subsequent bending of the overheated area. It is very well possible that the quality of the fiber degrades even before this critical temperature is reached. If that is the case, it could negatively impact the cleave quality or lead to inconsistencies in the ablation process. Should this cause any limitations on the overall quality of the final mirror profiles other stripping methods might need to be reconsidered.

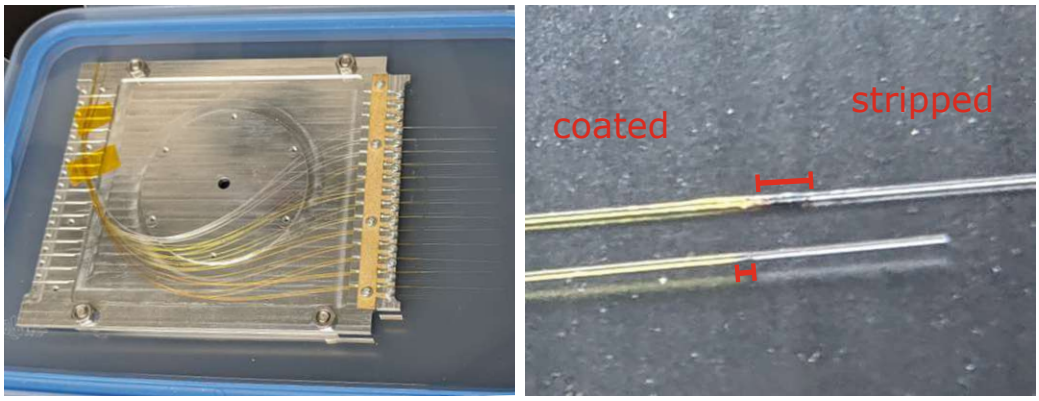

(a) (b)

Figure 4.1: (a) During the production process, the fibers are mounted in a "fiber holder". This enables convenient and save handling of the delicate fibers. The holders are designed to enable seamless integration into the whole production process. (b) The first step of the fiber production process is to strip the fibers of their polyimide coating. Covering the untreated part of fibers during the heat stripping process results in much smaller crossover sections of burnt residue. (lower fiber: covered; upper fiber: uncovered)

4.1.2 Fiber Cleaving

After the fibers have been stripped they can be cleaved. Cleaving is necessary to ensure that the end faces of the fibers are flat and smooth prior to the ablation process. This is essential as any defect in the fiber surface directly affect the quality

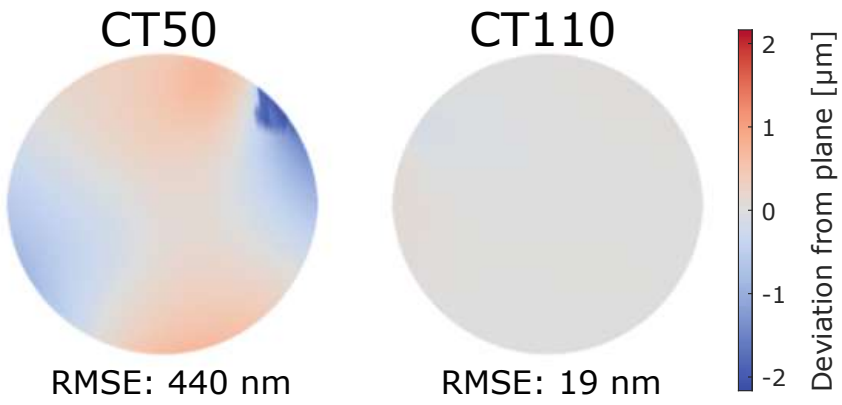

Figure 4.2: Comparison of two cleaved fiber end faces produced with two different fiber cleavers (Fujikura CT50 and Fujikura CT110). The images show the deviation from a perfect plane fit, the root mean square deviation is shown below each profile. The CT110-model clearly produces significantly flatter end faces with less defects.

of the final mirror. During the cleaving process the fiber is brought under tension by the fiber cleaver. A blade then creates a small intrusion on the edge of the fiber. This small crack propagates across the entire face of the fiber creating a, if done correctly, perfectly flat and defect free surface. After the fiber is cleaved, it is inspected with the white-light interferometer to ensure the quality of the fiber end face.

Initially a Fujikura CT50 fiber cleaver was used for cleaving the optical fibers. Inspection of the fiber end faces quickly revealed poor cleaving performance with surface defects at the micrometer scale, the same order of magnitude as the produced mirror profiles (see Fig. 4.2). As this severely limits the quality of the final surfaces a better cleaver had to be acquired. In contrast to the manually operated CT50, the Fujikura CT110 series operates fully automatic and allows for customization of a wide variety of cleaving parameters such as tension of the fiber during the cleaving process or the approach velocity of the cleaving blade. Even without much optimization the cleave profiles of the CT110 proved to be a significant improvement from the CT50-model.

Cleaving Angle

One additional consideration during the cleaving process is the resulting cleave angle θ between the cleaved surface and the plane perpendicular to the fiber axis. Any non-zero cleave angle result in an imperfect alignment of the final mirror structure with respect to the targeted fiber core as shown in Figure 4.3. This misalignment may dramatically reduce the coupling efficiency between the fiber mode and the cavity mode in the final FFPC. The overall coupling efficiency can be estimated via the formula [10]

$$T(\theta) = T_0 \exp(-\theta^2/\theta_e^2) \tag{4.1}$$

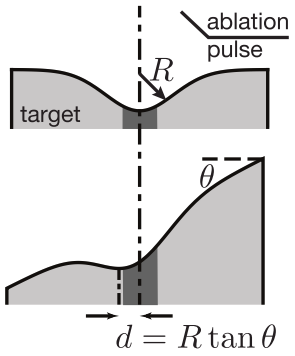

Figure 4.3: Any non-zero cleave angle results in a misalignment of the cavity mode and the fiber mode reducing the associated coupling efficiency. Figure adapted from [9]

where T_0 is the coupling efficiency without any tilt and θ_e is the angular tolerance which depends on the mode sizes of both the cavity and the fiber and on the radius of curvature of the mirror profile. Assuming a cleave angle of $\theta = 1°$ and using typical cavity parameters[2], equation (4.1) estimates a reduction in coupling efficiency of $\sim 5\,\%$.

To measure the cleave angle, the cleaved fiber surface is scanned with the white light interferometer. The resulting profile is then fit with a planar surface as shown in Figure 4.4a. From this fit the angle between the fiber surface and the imaging plane of the camera can be evaluated. The cleave angle cannot directly be determined from this single measurement alone, as multiple effects generally contribute to the measured offset angle. In addition to the cleave angle there generally is some non-zero offset between the fiber holder and the camera and some random noise introduced by inconsistent clamping of the fiber in the fiber holder. To disentangle those three contributions, the measurement can be repeated multiple times. Between each scan the fiber is rotated around its core. The characteristic intrusion point of the cleaver blade (yellow peaks in Fig. 4.4a) is used to track the rotation angle of the fiber. When plotted over the fiber rotation angle φ, the total measured tilt angle θ_x^{tot} along a given direction (e.g. the x-axis) show a characteristic oscillation of the form:

$$\theta_x^{tot}(\varphi) = \sin(\varphi) \cdot \theta^c + \Delta\theta_x + \delta\theta. \tag{4.2}$$

The amplitude of the oscillation can directly be contributed to the cleave angle θ^c. The offset $\Delta\theta_x$ corresponds to the offset in angles between camera and fiber holder along the x-axis. It is constant because the fiber holder alignment is not changed. The $\delta\theta$ therm describes any fluctuations between measurements caused by inconsistent mounting of the fiber. The tilt angle measured along the y-axis features the same oscillation with a phase shift of $\pi/2$ and a constant offset of $\Delta\theta_y$. Figure 4.4b depicts the results of a cleave angle measurement and clearly shows the expected oscillations. By fitting the data with a function in the form of (4.2), the cleave angle of

[2] $\lambda = 780\,\text{nm}$; $W_{\text{fiber}} = 2.5\,\mu\text{m}$; $W_{\text{cavity}} = 2\,\mu\text{m}$; $R = 150\,\mu\text{m}$

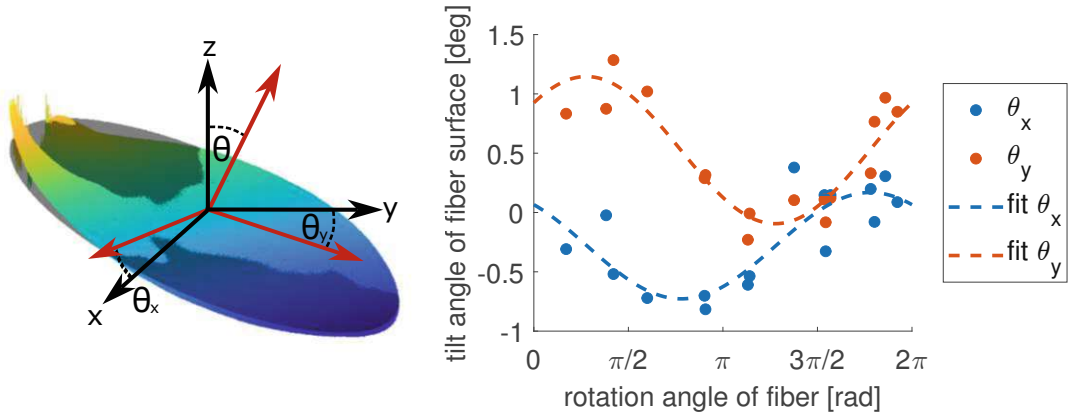

(a) (b)

Figure 4.4: Measurement of the cleave angle. (a) A plane is first fitted to the reconstructed fiber profile (gray surface). From the fit, the tilt angles θ_x and θ_y along the x- and y- axis are determined. (b) The tilt angles θ_x and θ_y are measured multiple times as a function of the rotation angle ϕ around the fiber center. The amplitude of the observed oscillation corresponds to the cleave angle θ^c, the constant offsets in x and y direction correspond to a constant offset angle between the fiber holder and the camera.

this particular fiber is evaluated as $\theta^c \approx 0.5°$ with mounting angles of $\Delta\theta_x \approx -0.2°$ and $\Delta\theta_y \approx 0.5°$. The cleave angle measured here was still created with the manual CT50 cleaver. The new automatic CT110-model promises even better results with average cleave angles of $< 0.3°$.

While the method presented above does work and produces good estimates for the different tilt angle contributions it is fairly labor intensive. This is because for each measurement the fiber has to be carefully rotated, manually repositioned on the camera and the profile has to be scanned and reconstructed. The whole process takes up to 10 minutes for each data point. It may thus not be practical to characterize every single fiber with this method but instead use it to characterize the performance of the cleaver or perform targeted inspection of selected fibers.

4.2 Fiber Ablation

Once the fibers are cleaved and the quality of the end face is deemed acceptable, the ablation process can commence.

Positioning of the Fiber

To ensure reproducibility of the ablation process the exact position of the fiber is first calibrated using the imaging setup described in section 3.2.1. For this purpose, an automatic routine has been added to the control program. The algorithm

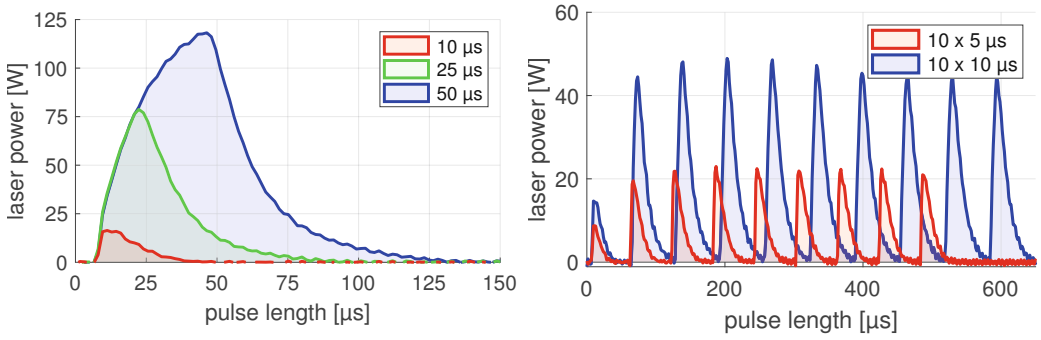

(a) (b)

Figure 4.5: During the ablation process either a single laser pulse (a) or a sequence of pulses (b) may be used to illuminate the surface.

takes an image of the fiber tip on the camera and subtracts an averaged signal of the background. An image recognition algorithm implemented with the *LabView Vision* package is then used to detect the circular edge of the fiber in the image. Once the edge is determined, the translation stages correct the position of the fiber automatically to center the fiber on the camera image. The positional calibration achieves an estimated accuracy of approximately 10 camera pixels, which is equivalent to 1.7 µm. This accuracy is primarily limited by the blurred appearance of the fiber edge in the camera image. The distance between camera and fiber is calibrated by adjusting the fiber position until the interference patterns are observed.

Once the fiber is fixed with respect to a reference point (i.e the center of the camera), the translation stages can then be moved to position the fiber in the center of the ablation beam. As the offset between camera and laser remains constant, the precise offset values each stage has to move only have to be calibrated once. This can either be done through iterative optimization or by comparing the shooting positions of previous runs and calculating backwards to evaluate the correct offset.

Ablation Sequence

Once the fiber is located at the appropriate position within the beam path the CO_2-laser is activated to start the ablation process. Depending on the set shooting parameters the laser may either apply a single pulse or a sequence of short pulses (Fig. 4.5). The maximum pulse length of a single pulses is typically $\lesssim 40 - 50\,\mu s$ as longer pulses deposit too much energy into the fiber resulting in large defects of the produced structures (Fig. 4.6c). Figures 4.6a and 4.6b show the fiber profiles before and after the ablation process.

4.3 Profile Characterization

After the ablation process, the mirror profiles are analyzed to evaluate the radius of curvature (ROC), useful mirror size, ellipticity and overall quality of the fabricated surface. For this the surfaces are first scanned and reconstructed using the white

(a) (b) (c)

Figure 4.6: Fiber surface before (a) and after a successful ablation process (b). (c) If too much energy is applied to the surface during the ablation process the resulting profile can show significant damage. The height difference between two interference maxima/minima is about 300 nm

light interferometer and phase unwrapping method introduced in section 3.2.1. The 3D surface data is then fit with a general bivariate 4th-degree polynomial. The fit is constrained to a circular area with a radius of 7.5 µm around the center of the hole. This threshold is added because expanding the fitting area too much introduces overfitting to regions farther from the mirror center. This in turn diminishes the accuracy of the fit at the center of the hole. Since the precise shape of the mirror center has a significantly greater influence on the overall mirror finesse than areas farther away it is crucial that the fit accurately captures the features of this area.

From the polynomial surface fit the coefficients of the quadratic components are then used to extract the parabolic part of the surface. As previously discussed in section 2.3.2 this quadratic part of the profile is a good approximation for the desired circular profile. With the quadratic coefficients, the major and minor axes of the paraboloid are then determined (see Fig. 4.7a). Figure 4.7b shows the 2D slices of the fabricated mirror profile and the 3D surface-fit along the those principle axes of the paraboloid. The ROC at the mirror center can easily be obtained from the quadratic coefficient $c_{\mathrm{maj/min}}$ along the respective axis. From (2.22) it directly follows that $R_{\mathrm{maj/min}} = 1/(2c_{\mathrm{maj/min}})$.

Getting an estimation for the effective mirror size is less straightforward. Other groups have used the width of a Gaussian fit as a measure for the effective mirror size. We do not use this definition for two reasons. The first reason is that while the Gaussian function qualitatively describes the ablated mirror profiles reasonably well, it fails to accurately capture the central, most significant area of the profile. The second reason is that the width of the Gaussian does not contain any information about the actual surface quality as local defects generally have little impact on the shape of the global fit function. Another method to estimate the useful mirror size is therefore used in this work. The effective mirror size is defined as the largest continuous region in which the deviation of the parabolic part of the polynomial fit from the actual surface is smaller than a given tolerance. Figure 4.8 shows the fit

error along the principle paraboloid axes as well as the tolerance threshold and the resulting mirror size. The value for the threshold has to be chosen such that small noise from the reconstruction process does not influence the size estimation while still capturing actual microscopic deformations of the surface. For scope of this work a threshold of 10 nm was found to be a reasonable compromise.

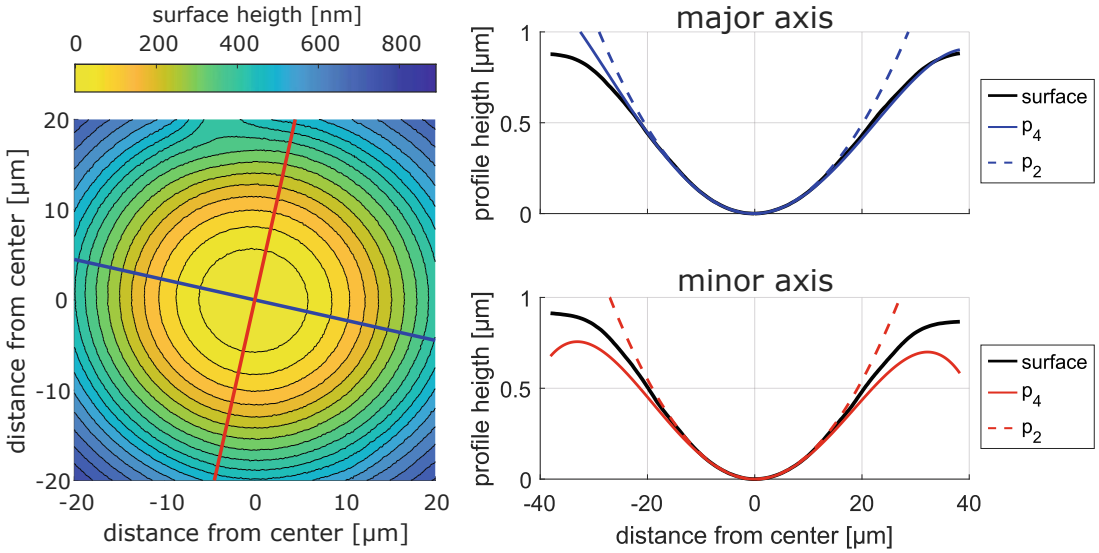

(a) (b)

Figure 4.7: (a) From the quadratic coefficients of the fitted 4th-degree polynomial, the major (blue) and minor (red) axes of the paraboloid are determined. The ROC and effective mirror size is evaluated along these axes. Figure (b) shows the 2D slices of the reconstructed surface and the quartic fit (p_4) as well as the quadratic component (p_2) of the fit.

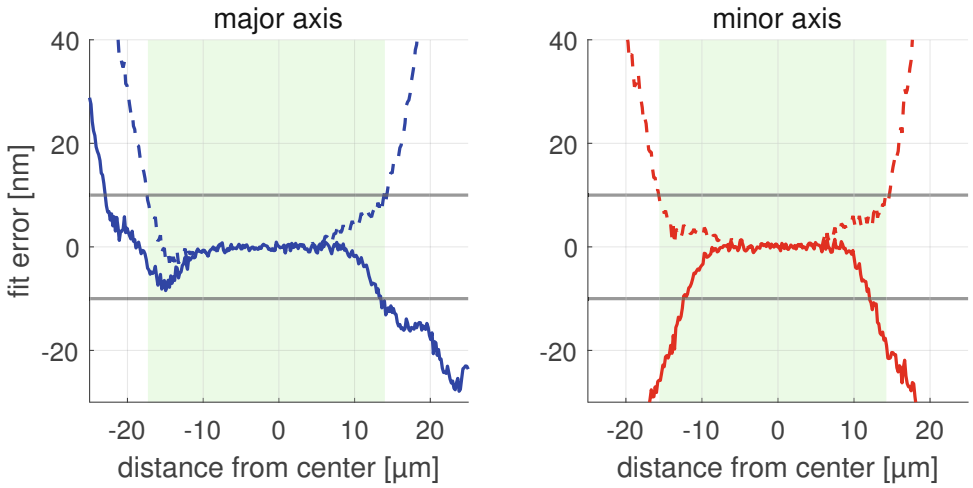

Figure 4.8: Deviation of the polynomial fit (solid lines) and the paraboloid (dashed lines) from the reconstructed surface profile. Effective mirror size is indicated by the shaded green area. The tolerance of 10 nm is indicated by the grey lines.

4.4 Coating

Before the fibers can be used to build a fiber cavity the mirror surfaces have to be coated to create the extremely high reflectivities required for a high finesse cavity. For a target finesse of $\mathcal{F} = 10^5$ the reflection and absorption losses have to be in the order of 10^{-3} %. To achieve these high reflectivities, the surfaces will be coated with alternating $\lambda/4$-layers of low (SiO_2) and high (Ta_2O_5) refractive indices. This will be done by an external company (*Laseroptik*). The finished fiber surfaces will then be inspected one last time to evaluate the final surface quality. The finesse of an individual fiber mirror can be characterized in combination with a planar mirror in a hemispherical configuration (see Fig. 2.2). Once the quality of the fiber is verified it may then be used to build high finesse FFPCs.

5 Prototype Production

In this chapter the most important results from different parameter scans and other tests of the production setup will be presented and discussed. A large portion of the testing process was performed with a fused silica glass plate instead of optical fibers. This is because the glass plate generally allows for much quicker iteration as no additional preparation and alignment process is required. Furthermore, the flat and homogeneous surface of the glass plate ensures consistent and reproducible testing conditions making it well suited for comparing the effects of different shooting parameters such as the energy of the ablation pulse and the axial position of the surface during the ablation process.

While sharing the same bulk material (SiO_2), the ablative properties of the optical fiber may differ from those of the glass window. This is because compared to the glass plate, the fiber has a much smaller surface area and less bulk material. Additionally, the influence that the doping of the different fiber layers has on the overall thermal properties of the fiber during the ablation process is also unknown. This means that the results of the glass plate tests are not be directly applicable to the optical fibers. Nevertheless, they provide reasonable starting estimates for further optimization.

5.1 Ablation of Glass Plate

For all tests involving the glass plate a large fused silica window[1] was mounted to the translation stages using a 2 axis mirror mount. Using the interferometry data of the camera the surface of the window was then aligned perfectly parallel to the camera.

Shooting Position

During the first tests, the effect of the position of the glass plate along the ablation-beam axis was investigated. This serves two purposes. Firstly, the precise offset between the camera imaging area and the focus point of the ablation laser is unknown and has to be calibrated with this measurement. Secondly, the beam width changes according to the Gaussian beam expansion around the waist of the ablation laser. Therefore by shooting at different axial positions the effect of different beam sizes on the produced structures can be analyzed.

[1] Thorlabs - WG42012

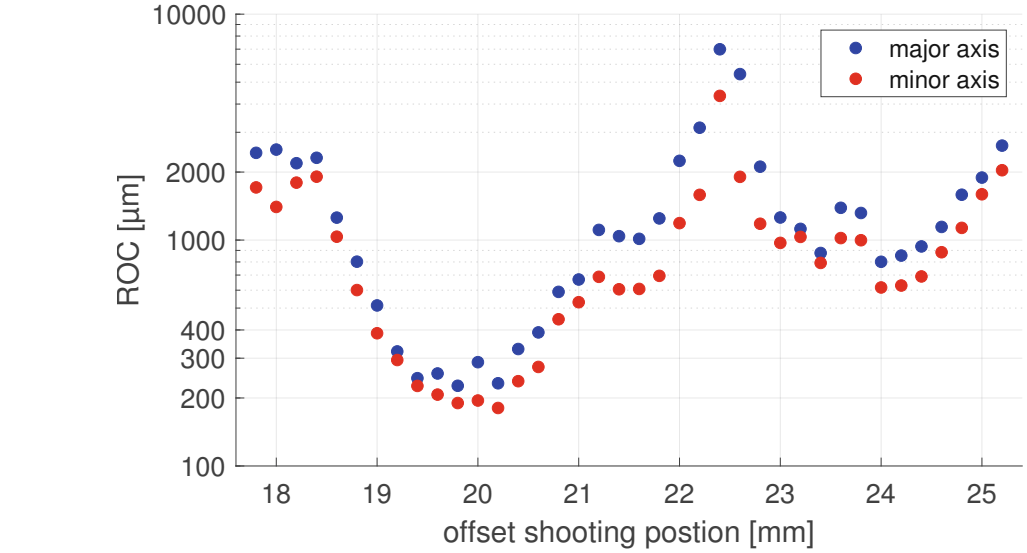

(a)

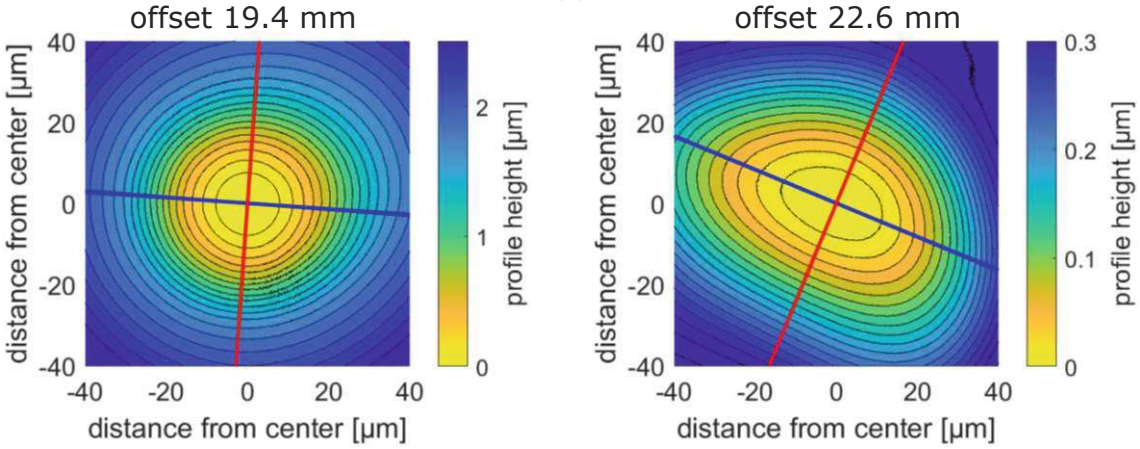

(b)

Figure 5.1: Result of shooting position scan. (a) ROC along the major and minor axes plotted over the shooting position along the beam axis. Instead of the expected minimum, the measured ROCs show a peak near the focal point of the laser beam. This peak is the result of an asymmetric intensity distribution in the proximity of the beam waist. (b) Contour plots of mirror profiles with indication of the principle axis of the fit paraboloid. Profiles with an offset of around 19.4 mm show much higher symmetry than profiles shot at an offset of 22.6 mm.

Figure 5.1a shows the measured radius of curvature (ROC) at different positions along the beam axis. Each profile was created using a single ablation pulse with a pulse length of 25 µs. The observed ROCs span over a large range of values between 180 µm and 7000 µm. In the resulting data we see an initial decrease in ROC as the offset between camera and shooting position is increased. This is consistent with the expected decrease in beam size as we move closer to the focus of the ablation laser. Similarly the ROC also increases at large offsets (> 24 mm) as we again move away from the focus. Between offsets of 20 mm to 24 mm we do not observe the expected

minimum associated with the beam waist. Instead we see an uncharacteristic peak in ROC that can only be understood by looking at the underlying surface profiles. Figure 5.1b shows a comparison of two profiles at 19.4 mm and 22.6 mm respectively. In contrast to the profile at 19.4 mm which is reasonably well described by the expected Gaussian shape, the profile at 22.6 mm shows significant asymmetry. The asymmetry is consistently observed in this region and most likely a result of a non-Gaussian intensity distributions in the ablation beam. This could either be caused trough the presence of higher order modes in the ablation beam, through optical phenomena like astigmatism and optical aberrations or through a combination of those effects. To avoid any asymmetry in the final mirror profiles all further testing was therefore performed at or around a y-offset of 19.4 mm as this was found to be the region that produced the most symmetrical structures.

Illumination Time

To study the effect of the illumination time on the produced profiles a series of short pulses rather than a single pulse is used. As discussed in section 3.1.1 the intensity at rising edge of the pulse is highly non-linear in the short time regimes used in the fabrication process. Therefore using a series of smaller pulses allows for finer control and results in more linear scaling of the total deposited energy over time.

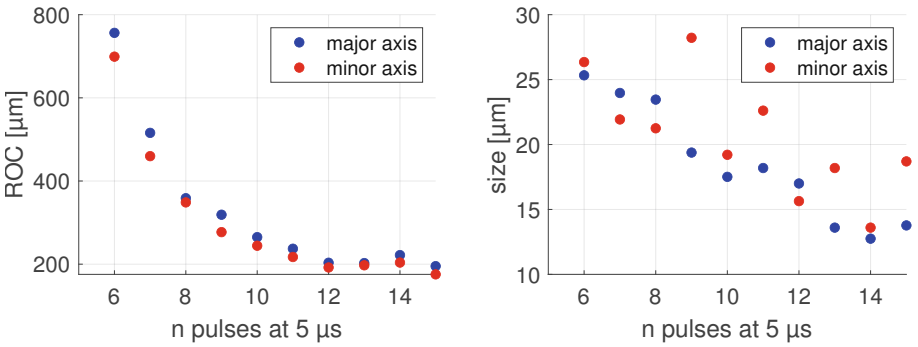

Figure 5.2: Results of the illumination time scan. Measured ROC and effective mirror size are plotted over the number of 5 µs pulses that were applied during the ablation process.

Figure 5.2 shows the measured ROCs and estimated mirror sizes of a test series using an increasing number of 5 µs pulses. The time delay between each pulse was set to 55 µs. The data shows that the ROC decreases with longer total illumination times. This is expected as small total energy deposition during the ablation process only produce shallow holes with a larger ROC. Long illumination times deposit more energy into the material resulting in deeper structures with smaller ROCs. After around 12 pulses the curve flattens at a ROC of around 200 µm. Additional pulses no longer lead to a further reduction in ROC. From this point on the profile shape is limited by the finite size of the ablation beam. The effective mirror size defined in section 4.3 also decreases with more ablation pulses. This is a result of two effects. Firstly, as discussed in section 2.3.2, as the width of the fabricated hole

decreases, so does the area in which a paraboloid used for size estimation is a good approximation for the overall profile. Secondly, as discussed in section 2.3.1 longer illumination times may also lead to increasing non-linear thermal effects during the ablation process. This would lead to a larger deviation of the produced surface from the predicted Gaussian form and a thus reduce the region in which the parabola is a good description of the mirror profile.

Reproducibility

The final test on the glass plate investigates the consistency and reproducibility of the ablation process. For this measurement 10 mirror profiles were created using the same set of parameters for each shot. Similar to the illumination time test 12 pulses with pulse lengths of 5 µs and a pulse separation of 55 µs were used to create each profile. Figure 5.3 shows the measured ROC, the resulting ellipticity $\varepsilon = \sqrt{1 - R_{\text{min}}/R_{\text{maj}}}$ and the effective mirror size. Table 5.1 lists the mean values and standard deviations of the measured data. The observed ROC is consistently evaluated at around 180 µm for both axes with a standard deviation of about 10%. The estimated mirror size shows significantly larger variations of more than 25% especially along the major axis. This is somewhat expected as the method for determining the effective mirror size is inherently more sensitive to noise or small defects in the mirror surface. The average ellipticity is determined to be 0.18 which indicates very high symmetry of the produced profiles.

	major axis	minor axis
ROC [µm]	183 ± 20	178 ± 18
Size [µm]	24 ± 8	17 ± 4
Ellipticity	0.18 ± 0.04	

Table 5.1: Mean values and standard deviation of ROC, effective mirror size and ellipticity measured from 10 independent shots using the same ablation parameters.

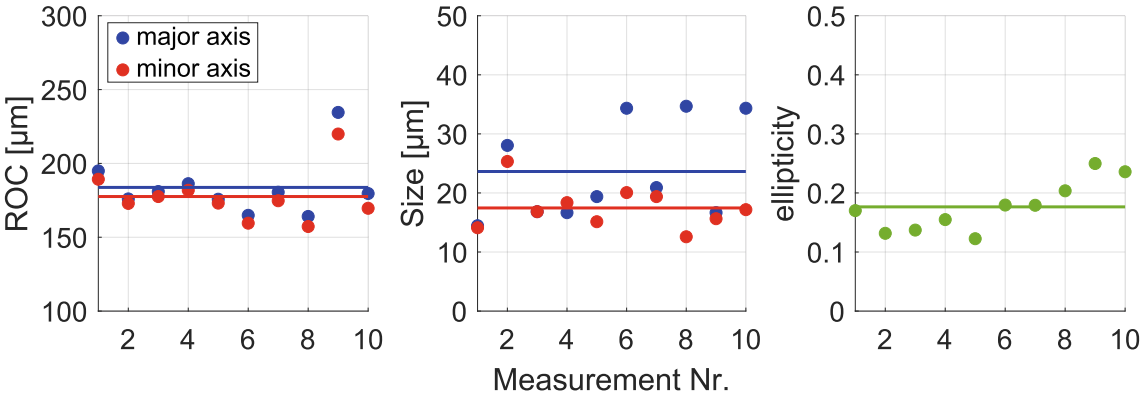

Figure 5.3: ROC, effective mirror size and ellipticity of 10 shots each created with 12 pulses of 5 µs. Solid lines indicate the mean values.

5.2 Ablation of Fiber Facets

Extensive testing of the fiber ablation process has not been performed yet. Therefore this section will present some preliminary results showcasing the current status of the development process as well as outlining some of the potential challenges of further optimization.

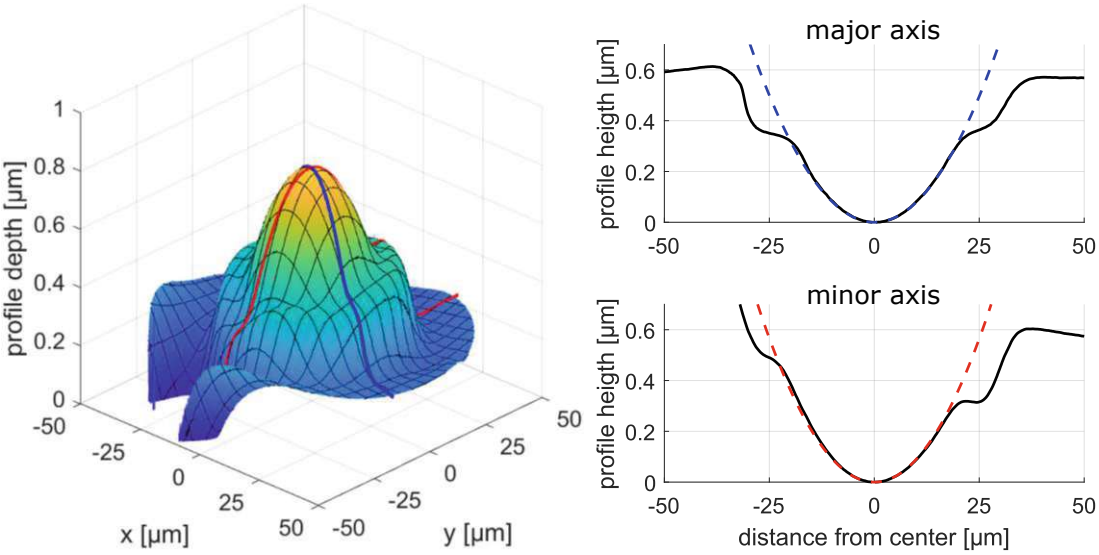

Figure 5.4: Ablation profile of a multi-mode fiber. The center of the profile is well described by the expected paraboloid. A significant defect is observed at a radial distance of 25 µm from the center. The location of the defect corresponds to the core-cladding transition of the fiber. The slight asymmetry observed along the minor mirror axis is a result of the of the defect at the blade impact point of the cleaver.

Multi-mode Fiber

The multi-mode fibers we are using are step index fibers with a core diameter of 50µm. The fibers are first stripped, and cleaved as outlined in section 4.1 before being installed in the ablation setup.

Figure 5.4 shows the profile and slices along the principle axes resulting from an ablation sequence using 7 pulses with a pulse length of 5µs. The ROCs of the profile are evaluated as $R_{\mathrm{maj}} = 627\,\mu\mathrm{m}$ and $R_{\mathrm{min}} = 552\,\mu\mathrm{m}$. The respective mirror sizes are 36 µm along the major and 29 µm along the minor axis. The ellipticity of the profile is 0.34. All together these results are in good agreement with previous results obtained during the glass plate tests (fig5.2).

From figure 5.4 we see a circular plateau in the profile at a distance of 25 µm from the center. This structure has been observed at the same location for all multi-mode fiber tests irrespective of the exact shooting parameters. The size, circular shape and location of the defect correspond precisely to the expected position of the boundary

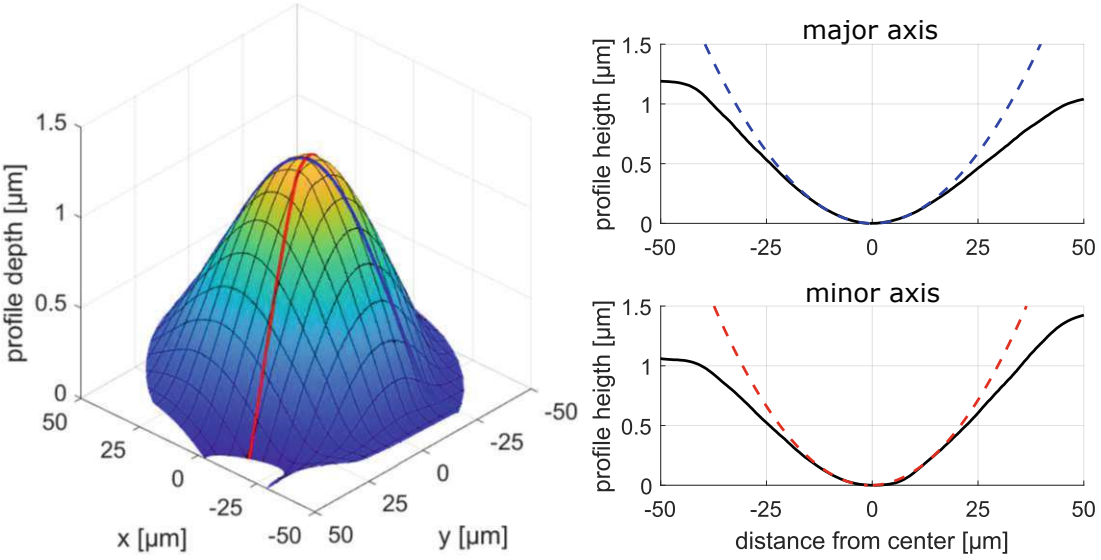

Figure 5.5: Ablation profile of a single-mode fiber. The center of the profile is well described by the expected paraboloid. The defect caused by the core-cladding transition layer is much less pronounced in single-mode fibers than in multi-mode fibers.

layer between core and cladding in the multi-mode fiber. It is thus highly likely that this transition layer has some significant impact on the ablative properties of the fiber.

Single-mode Fiber

The single-mode fibers used for testing have a smaller core radius of only 5 µm. The effect of the core-cladding transition observed for the multi-mode fiber is therefore much less pronounced and much more difficult to pinpoint among other defects in the profile.

Figure 5.5 shows the profile and 2D slices along the principle axes of a single-mode fiber that was produced with a single 25 µs ablation pulse. The measured ROCs are $R_{\text{maj}} = 524\,\mu\text{m}$ and $R_{\text{min}} = 454\,\mu\text{m}$ with mirror sizes of 30 µm along the major and 16 µm along the minor axis and an ellipticity of 0.36. From figure 5.5 alone the effect of the fiber core is only barely discernibly. Figure 5.6 shows the difference between the scanned surface and the fit surface. Here the fiber core is clearly visible as a deviation of the actual surface from the polynomial fit. As expected, the impact of the small single-mode fiber core on the overall mirror profile, while noticeable, is much less severe than for the lager multi-mode core.

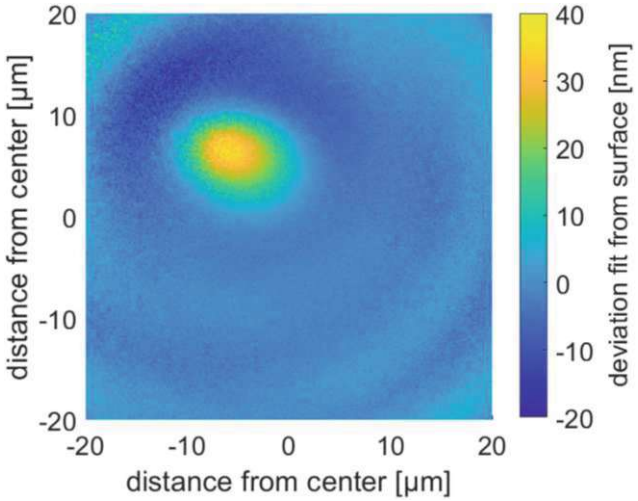

Figure 5.6: Deviation of the surface fit from the reconstructed single-mode profile. The yellow spot with the largest deviation corresponds to the position of the fiber core. Because of a non-optimized shooting offset, the fiber core is slightly off center with respect to the mirror structure.

6 Conclusion and Outlook

6.1 Summary

This work provides a detailed description of the different techniques and processes involved in the production of high finesse fiber mirrors using CO_2-laser ablation. These fiber mirrors are essential for building high finesse fiber Fabry-Pérot cavities which unlock new possibilities for exploring the rich and interesting field of cavity quantum-electrodynamics. The presented ablation setup was characterized in a series of tests to investigate both the capabilities of the current production setup as well as study the effects of different ablation parameters on the final mirror profiles.

The first ablation profiles were fabricated onto a fused silica window instead of optical fibers. The results of these initial tests show that the current setup can consistently produce mirror profiles with ROCs ranging from a few thousand micrometers down to around 16 µm. The lower limit for the ROC is mainly set by the finite size of the ablation beam. The observed ellipticity of the profiles is as small as 0.2 which is even lower than what other groups have reported [20]. The effective mirror sizes of the profiles range from 20 µm for the smallest ROCs to about 35 µm for profiles with larger ROCs. Altogether, our results demonstrate that we can already produce mirror surfaces on par with those from leading research groups, using an ablation setup with the potential to even surpass the current state of the art.

The ablation of fiber surfaces has not been tested extensively yet. However, the first prototype results already seem promising and in reasonable agreement with the data from the previous glass plate tests. One major challenge moving forward may be the significant impact that the different fiber layers were observed to have on the final mirror profile. The defects observed at the boundary between fiber-core and cladding could potentially pose a significant limitation on the achievable mirror size and quality.

Nevertheless, we are confident that, with the current setup, we will soon be able to produce fiber mirrors of equal if not better quality than the ones we are currently using. This would allow us to build fiber cavities with finesses of more than 50 000 and lengths exceeding 100 µm. This upgrade will significantly enhance our experimental platform, allowing us to explore a broader range of many-body physics regimes in terms of system size and coupling strength.

6.2 Future Improvements

To even further enhance the quality of our fiber mirrors and eventually construct fiber cavities with finesses exceeding 100 000, we will need to continuously refine and improve our production setup and processes. Two of the most promising upgrades to the ablation setup are the installation of an acousto-optic modulator (AOM) to regulate the ablation laser power and the implementation of the dot milling technique.

Installation of AOM

One of the major limitations of the current ablation setup is the poor control over the laser power during the ablation process. The CO_2-laser used in our setup can only be operated at full power (55 W) and quickly burns any fiber tip for ablation pulses lasting longer than only a few tens of microseconds. Reducing the optical power of the ablation pulse would allow for a significantly longer and more gentle ablation process which will hopefully increase the quality of the final mirror surface. An acousto-optic modulator is currently being installed in the laser setup to provide precise control over the optical power of the laser. By tuning the RF power applied to the AOM, its diffraction efficiency and in extension the power of the ablation laser can be tuned over a continuous range from zero up to the maximum laser power. This will provide precise control over the intensity curve of our ablation pulses.

Dot milling

At some point the production setup will most likely be expanded to also facilitate dot milling laser ablation. In the dot milling process the mirror surface is shaped not by a single ablation pulse but by multiple spatially separated pulses. This technique provides much finer control of the fabricated mirror structures as it is not limited by the intensity distribution of a Gaussian ablation beam. The success of the dot milling method has already been demonstrated by other groups [14]. Implementing this technique would unlock the potential of fabricating high finesse fiber mirrors with truly fully customizable surface geometries.

Bibliography

[1] *DIAMONDC-55 Liquid-Cooled OEM Laser Operator's Manual*. Coherent Inc. 2018.

[2] H. J. Eichler, J. Eichler, and O. Lux. *Lasers - Basics, Advances and Applications*. Springer Cham, 2018. ISBN: 978-3-319-99895-4. DOI: 10.1007/978-3-319-99895-4.

[3] M. D. Feit and A. M. Rubenchik. "Modeling of Laser Induced Damage in NIF UV Optics". In: (2001). DOI: 10.2172/15002111.

[4] C. Grave. "Towards the fabrication of fiber-based Fabry Perot cavities". master's thesis. TU Wien, 2024.

[5] M. A. Herráez et al. "Fast two-dimensional phase-unwrapping algorithm based on sorting by reliability following a noncontinuous path". In: *Appl. Opt.* 41.35 (2002). DOI: 10.1364/AO.41.007437.

[6] D. Hunger et al. "A fiber Fabry–Perot cavity with high finesse". In: *New Journal of Physics* 12.6 (2010). DOI: 10.1088/1367-2630/12/6/065038.

[7] D. Hunger et al. "Laser micro-fabrication of concave, low-roughness features in silica". In: *AIP Advances* 2.1 (2012). DOI: 10.1063/1.3679721.

[8] I. Dotsenko. "Single atoms on demand for cavity QED experiments". PhD thesis. Rheinische Friedrich-Wilhelms-Universität Bonn, 2007. URL: https://hdl.handle.net/20.500.11811/3091.

[9] J. C. Gallego Fernández. "Strong Coupling between Small Atomic Ensembles and an Open Fiber Cavity". PhD thesis. Rheinische Friedrich-Wilhelms-Universität Bonn, 2018.

[10] W. B. Joyce and B. C. DeLoach. "Alignment of Gaussian beams". In: *Appl. Opt.* 23.23 (1984). DOI: 10.1364/AO.23.004187.

[11] M. F. Kasim. *Fast 2D phase unwrapping implementation in MATLAB*. https://github.com/mfkasim1/unwrap_phase. Accessed: December 10, 2024. 2017.

[12] R. Kitamura, L. Pilon, and M. Jonasz. "Optical constants of silica glass from extreme ultraviolet to far infrared at near room temperature". In: *Appl. Opt.* 46.33 (2007). DOI: 10.1364/AO.46.008118.

[13] M. Kubista. "A New Fiber Mirror Production Setup". master's thesis. Rheinische FriedrichWilhelms-Universität Bonn, 2023.

[14] K. Ott. "Towards a squeezing-enhanced atomic clock on a chip". PhD thesis. Université Pierre et Marie Curie - Paris VI, Sept. 2016. URL: https://theses.hal.science/tel-01452767.

[15] H. Pfeifer et al. “Achievements and perspectives of optical fiber Fabry–Perot cavities”. In: *Applied physics. B, Lasers and optics* 128.2 (2022). ISSN: 0946-2171.

[16] A. Reiserer and G. Rempe. “Cavity-based quantum networks with single atoms and optical photons”. In: *Rev. Mod. Phys.* 87 (2015). DOI: 10.1103/RevModPhys.87.1379.

[17] I. Safa. “Fiber Fabry-Pérot Cavity for Enhanced Atom-Cavity Coupling”. internship report. TU Wien, 2023.

[18] M. C. Teich. *Fundamentals of photonics*. eng. Third edition. Wiley series in pure and applied optics. Hoboken, N.J.: Wiley, 2019. ISBN: 1119702119.

[19] N. Thau. “Optical fiber cavities”. master’s thesis. Rheinische FriedrichWilhelms-Universität Bonn, 2012.

[20] M. Uphoff. “Optical microcavities for quantum communication with single atoms”. PhD thesis. Technische Universität München, 2017.

[21] M. Uphoff et al. “Frequency splitting of polarization eigenmodes in microscopic Fabry–Perot cavities”. In: *New Journal of Physics* 17.1 (2015), p. 013053. DOI: 10.1088/1367-2630/17/1/013053.

List of Figures

List of Tables